

# Detecting, tracking, and eliminating drift in quantum information processors

Timothy Proctor,<sup>1,\*</sup> Melissa Revelle,<sup>2</sup> Erik Nielsen,<sup>1</sup> Kenneth Rudinger,<sup>1</sup>  
Daniel Lobser,<sup>2</sup> Peter Maunz,<sup>2</sup> Robin Blume-Kohout,<sup>1</sup> and Kevin Young<sup>1</sup>

<sup>1</sup>*Quantum Performance Laboratory, Sandia National Laboratories,  
Albuquerque, NM 87185 and Livermore, CA 94550*

<sup>2</sup>*Sandia National Laboratories, Albuquerque, NM 87185*

(Dated: September 2, 2022)

If quantum information processors (QIPs) are ever to fulfill their potential, the diverse errors that impact them must be understood and suppressed. But errors fluctuate over time in most processors and the most widely used tools for characterizing them assume static error modes and rates. This mismatch can cause unheralded failures, misidentified error modes, and significant waste of experimental effort. Here, we demonstrate a fast spectral analysis technique for resolving time dependence in QIPs. Our method is simple and statistically sound, and it can be applied to time-series data from any repeated QIP experiment. We use data from both numerical simulations and trapped-ion qubit experiments to show how our method can resolve time dependence when coupled to popular characterization protocols, including randomized benchmarking, gate set tomography, and Ramsey spectroscopy. In the experiments, we detected instability and localized its source, then implemented drift control techniques to mitigate it, and finally used our methods to demonstrate that the instability had been eliminated.

Recent years have seen rapid advances in quantum information processors (QIPs). Testbed processors containing 10s of qubits are becoming commonplace [1–6] and error rates are being steadily suppressed [1, 7], fueling optimism that useful quantum computations will soon be performed. Improved theories and models of the types and causes of errors in QIPs have played a crucial role in these advances. These new insights have been made possible by a range of powerful device characterization protocols [7–19] that allow scientists to probe and study QIP behavior. But almost all of these techniques assume that the QIP is stable – that data taken over a second or an hour reflect some constant property of the processor. They can malfunction badly if the actual error mechanisms are time-dependent [20–26].

Yet temporal instability in QIPs is ubiquitous [24–36]. The control fields used to drive logic gates generally drift. Solid-state qubit frequencies often slowly vary,  $T_1$  times can change abruptly, and low-frequency  $1/f^\alpha$  noise is common. Laboratory equipment produces strongly oscillating noise, including 50 Hz/60 Hz line noise and  $\sim 1$  Hz mechanical vibrations from refrigerator pumps. These intrinsically time-dependent error mechanisms are becoming more and more important as technological improvements suppress stable and better-understood errors. As a result, techniques to characterize QIPs with time-dependent behavior are becoming increasingly necessary.

In this article we demonstrate a general, flexible and powerful methodology for detecting and measuring time-dependent errors in QIPs. The core of our techniques can be applied to *time-series* data from any set of repeated quantum circuits, so they can be applied to most QIP experiments with only superficial adaptations. This means that they can be used for routine, consistent stability analyses across QIP platforms, complementing tools that

focus on specific types of drift [27–30, 37–47]. Moreover, using data from both simulations and experiments, we demonstrate that our methods can be used to upgrade standard characterization protocols – including randomized benchmarking [12–19] and gate set tomography [7–10] – into time-resolved techniques.

Our experiments were performed using a  $^{171}\text{Yb}^+$  ion qubit suspended above a linear surface-electrode trap [7] and controlled using resonant microwaves (details of the experiment are described in the Methods). We used this platform to illustrate the various stages of our technique as applied to a simple set of Ramsey spectroscopy circuits. These circuits consist of preparing a qubit on the  $\hat{x}$  axis of the Bloch sphere, waiting for a time  $lt_w$  ( $l = 1, 2, 4, \dots, 8192$ ,  $t_w \approx 400 \mu\text{s}$ ), and measuring along the  $\hat{y}$  axis. We then implemented high-precision, time-resolved tomography of the microwave gates. We detected a small instability in the gates, isolated its source, and modified the experiment design to mitigate the discovered instability. By then repeating the experiment on the stabilized qubit, we were able to show both improved error rates and a complete absence of detectable drift.

## RESULTS

**Instability in quantum circuits.** Experiments to characterize QIPs almost always involve choosing some quantum circuits and running them many times. The resulting data is usually recorded as counts [7–19] for each circuit – *i.e.*, the total number of times each outcome was observed for each circuit. Dividing these counts by the total number of trials yields *frequencies* that serve as good estimates of the corresponding probabilities *averaged* over the duration of the experiment. But if the QIP’s properties vary over that duration, then the counts

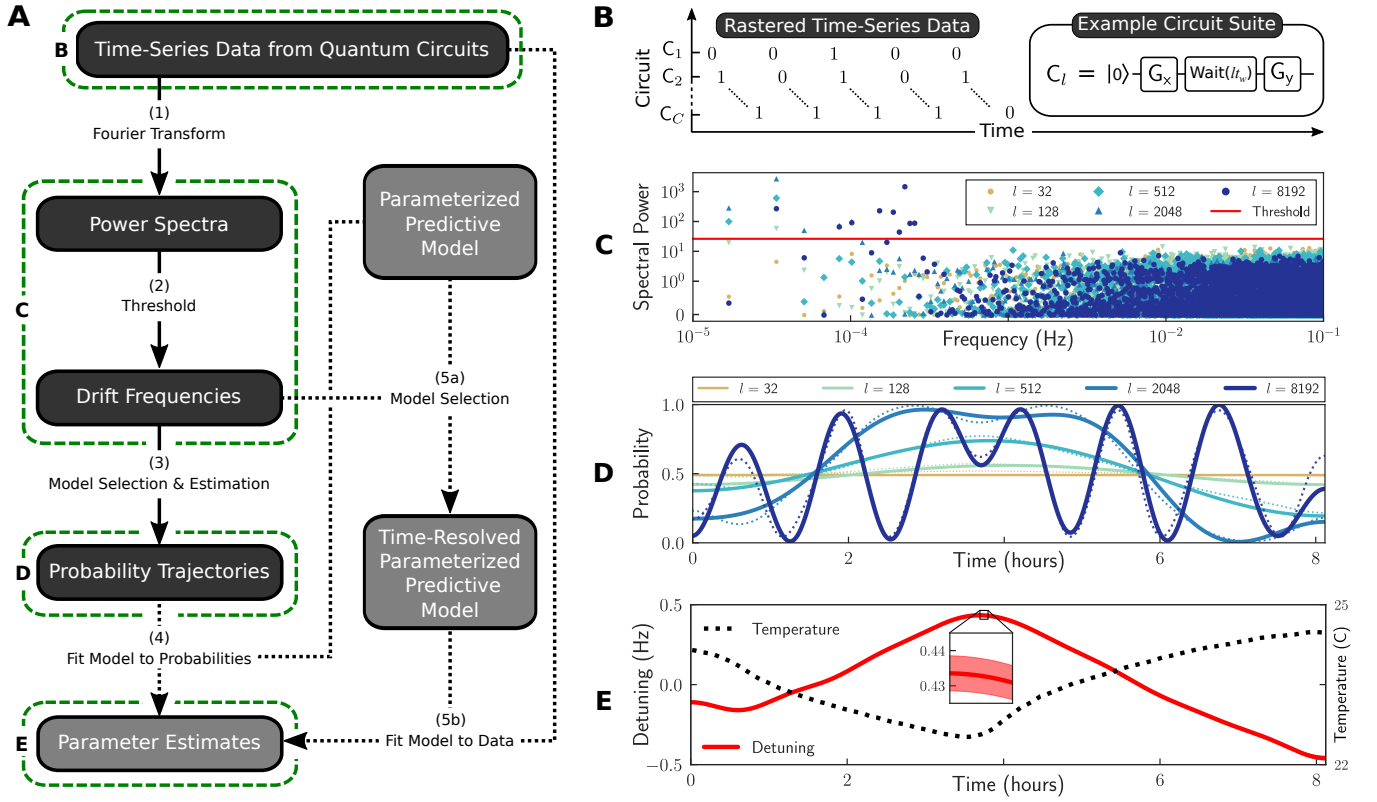


**FIG. 1. Diagnosing time-dependent errors in a quantum information processor.** **A.** A flowchart of our methodology for detecting and quantifying drift in a QIP, using time-series data from quantum circuits. The core steps (1–3) detect instability, identify the dominant frequencies in any drift, and estimate the circuit outcome probabilities over time. Additional steps (4 and/or 5) estimate time-varying parameters (*e.g.*, error rates) whenever a time-independent parameterized model is provided for predicting circuit outcomes. **B.** An example of circuits on which this technique can be implemented – Ramsey circuits with a variable wait time  $l t_w$  – as well as an illustration of data obtained by “rastering” (each circuit is performed once in sequence and this sequence is repeated  $N$  times). **C–E.** Results from performing these Ramsey circuits on a  $^{171}\text{Yb}^+$  ion qubit ( $l = 1, 2, 4, \dots, 8192$ ,  $t_w \approx 400 \mu\text{s}$ ,  $N = 6000$ ), and the corresponding stages of the flowchart. **C.** The power spectra observed in this experiment for selected values of  $l$ . Frequencies with power above the threshold almost certainly appear in the true time-dependent circuit probabilities,  $p_l(t)$ . **D.** Estimates of the probability trajectories (unbroken lines are estimates from step 3 of the flowchart; dotted lines are the probabilities implied by the time-resolved detuning estimate shown in E). **E.** The standard Ramsey model  $p_l(t) = A + B \sin(2\pi l t_w \Omega)$ , where  $\Omega$  is the qubit detuning, is promoted to a time-resolved parameterized model (step 5a) and fit to the data (step 5b), resulting in a time-resolved detuning estimate. The shaded area in the inset is a  $2\sigma$  confidence region. The estimated detuning closely mirrors ambient laboratory temperature.

do not capture all the information available in the data, and time-averaged probabilities do not faithfully describe the QIP’s behavior. The counts may then be irreconcilable with *any* model for the QIP that assumes time-independent states (density matrices) and gates (process matrices). This discrepancy results in failed or unreliable tomography and benchmarking experiments [20–26].

Time-resolved analysis can be enabled by simply recording the observed outcomes for each circuit in sequence, rather than compressing them into counts. We call the sequence of outcomes  $\vec{x} = (x_1, x_2, \dots, x_N)$  obtained at  $N$  data collection times  $t_1, t_2, \dots, t_N$  a *clickstream*. There is one clickstream for each circuit. We focus on circuits with binary 0/1 outcomes (the general case of  $M$ -outcome measurements is addressed in the Methods), and on data obtained by *rastering* through

the circuits. Rastering means running each circuit once in sequence, then repeating that process until we have accumulated  $N$  clicks per circuit (see Fig. 1B). Under these conditions, the clickstream associated with each circuit is a string of bits, at successive times, each of which is sampled from a probability distribution over  $\{0, 1\}$  that *may* vary with time. If this probability distribution *does* vary over time, then we say that the circuit is temporally unstable. In this article we present methods for detecting and quantifying temporal instability, using clickstream data, which are summarized in the flowchart of Fig. 1A.

Our methodology is based on transforming the data to the frequency domain and then thresholding the resultant power spectra (steps 1–2, Fig. 1A). From this foundation we generate a hierarchy of outputs: yes/no instability detection and a set of drift frequencies if instability is de-

tected; estimates of the circuit probability trajectories; and estimates of time-resolved parameters in a device model. To motivate this strategy, we first highlight some unusual aspects of this data analysis problem. Formally, the clickstream  $\vec{x}$  from a circuit consists of one draw from a vector of independent Bernoulli (coin) random variables  $\vec{X} = (X_1, X_2, \dots, X_N)$  with biases  $\vec{p} = (p_1, p_2, \dots, p_N)$ , where  $p_i = p(t_i)$  is the instantaneous probability to obtain 1 at the  $i^{\text{th}}$  repetition time of this circuit, and  $p(\cdot)$  is the continuous-time probability trajectory. The naive strategy for quantifying instability is to estimate  $\vec{p}$  from  $\vec{x}$  assuming nothing about its form. However,  $\vec{p}$  consists of  $N$  independent probabilities and there are only  $N$  bits from which to estimate them, so this strategy is evidently flawed. The best fit is always  $\vec{p} = \vec{x}$ , which is a probability jumping between 0 and 1, even if the data seems typical of draws from a fixed coin. This is overfitting.

To avoid overfitting we must assume that  $\vec{p}$  is within some relatively small subset of all possible probability traces. Common causes of time variation in QIPs are not restricted to any particular portion of the frequency spectrum, but they are typically sparse in the frequency domain, *i.e.*, their power is concentrated into a small range of frequencies. For example, step changes and  $1/f^\alpha$  noise have power concentrated at low frequencies, while 50 Hz/60 Hz line noise has an isolated peak, perhaps accompanied by harmonics. Broad-spectrum noise *does* appear in QIP systems, but precisely because it has an approximately flat spectrum, it acts like white noise – which produces stationary stochastic errors that existing techniques are well-suited to deal with. So we model variations as sparse in the frequency domain, but otherwise arbitrary.

**Detecting instability.** The expected value of a clickstream ( $\vec{X}$ ) is the probability trajectory ( $\vec{p}$ ), and this also holds in the frequency domain. That is,  $\mathbb{E}[\vec{X}] = \vec{p}$  where  $\mathbb{E}[\cdot]$  is the expectation value and  $\vec{v}$  denotes the Fourier transform of a vector  $\vec{v}$  (there are multiple discrete Fourier transforms and the exact transform used is not important, except that we require that  $\tilde{v} = F\vec{v}$  where  $F$  is an orthogonal matrix: see the Methods). In the time domain, each  $x_i$  (a single bit) is a very low-precision estimate of  $p_i$ . In the frequency domain, each  $\tilde{x}_\omega$  is the weighted sum of  $N$  bits, so the strong, independent shot noise inherent in each bit is largely averaged out and any non-zero  $\tilde{p}_\omega$  is highlighted. Of course, simply converting to the frequency domain cannot reduce the total amount of shot noise in the data. To take advantage of this intuitive noise suppression we need a principled method for deciding when a data mode  $\tilde{x}_\omega$  is sufficiently close to zero that it is *consistent* with  $\tilde{p}_\omega = 0$  (it is impossible to prove that this holds exactly). One option is to use a regularized estimator inspired by compressed sensing [48], but we take a different route, as this problem naturally fits within the flexible and statistically transparent

framework of statistical hypothesis testing [49, 50].

We start from the *null hypothesis* that all the probabilities are constant – *i.e.*,  $\tilde{p}_\omega = 0$  for every  $\omega > 0$  and every circuit. Then, for each  $\omega$  and each circuit we conclude that  $|\tilde{p}_\omega| > 0$  only if  $|\tilde{x}_\omega|$  is so large that it is inconsistent with the null hypothesis at a pre-specified significance level  $\alpha$ . If we standardize  $\vec{x}$ , by subtracting its mean and dividing by its variance, then this procedure becomes particularly transparent: if the probability trace is constant, then the marginal distribution of each Fourier component  $\tilde{X}_\omega$  is approximately normal, and so its power  $|\tilde{X}_\omega|^2$  is  $\chi_1^2$  distributed. So if  $\tilde{x}_\omega^2$  is larger than the  $\alpha$ -percentile of a  $\chi_1^2$  distribution, then it is inconsistent with  $\tilde{p}_\omega = 0$ . To test at every frequency in every circuit requires many hypothesis tests. Using standard techniques [49, 50], we set an  $\alpha$ -significance power threshold such that the probability of falsely concluding that  $|\tilde{p}_\omega| > 0$  at *any* frequency and for *any* circuit is at most  $\alpha$  (*i.e.*, we seek strong control of the family-wise error rate – see the Methods).

We now demonstrate this drift detection method with data from the Ramsey experiment described above. We performed 6000 rasters through the circuits of Fig. 1B over approximately 8 hours. A representative subset of the power spectra for this data are shown in Fig. 1C, as well as the  $\alpha$ -significance threshold for  $\alpha = 5\%$ . The spectra for circuits containing long wait times exhibit power above the detection threshold. These data are therefore inconsistent with constant probabilities, so instability was detected. Ramsey circuits are predominantly sensitive to phase accumulation while the qubit is idling, caused by detuning between the qubit and the control field frequencies. It is therefore reasonable to assume that it is this detuning that is drifting. The detected frequencies range from the lowest Fourier basis frequency for this experiment duration – approximately 15  $\mu\text{Hz}$  – up to approximately 250  $\mu\text{Hz}$ . The largest power is more than 1700 standard deviations above the expected value under the null hypothesis, which is overwhelming evidence of temporal instability.

**Quantifying instability.** Statistically significant evidence in data for time-varying probabilities does *not* directly imply anything about the size of the detected instability. If enough data is taken, then even the smallest instabilities will almost surely be detected by our methods. We can quantify instability in any circuit by the size of the variations in its outcome probabilities. We can measure this size by estimating the probability trajectory  $\vec{p}$  for each circuit (step 3, Fig. 1A). As noted above, the unregularized best-fit estimate of  $\vec{p}$  is the observed bit-string  $\vec{x}$ , which is absurd. To regularize this estimate, we adopt a model-selection framework: we start from the model of a constant probability and include only those frequencies that have been identified via the hypothesis testing as being components of  $\vec{p}$ . Specifically, we construct the time-

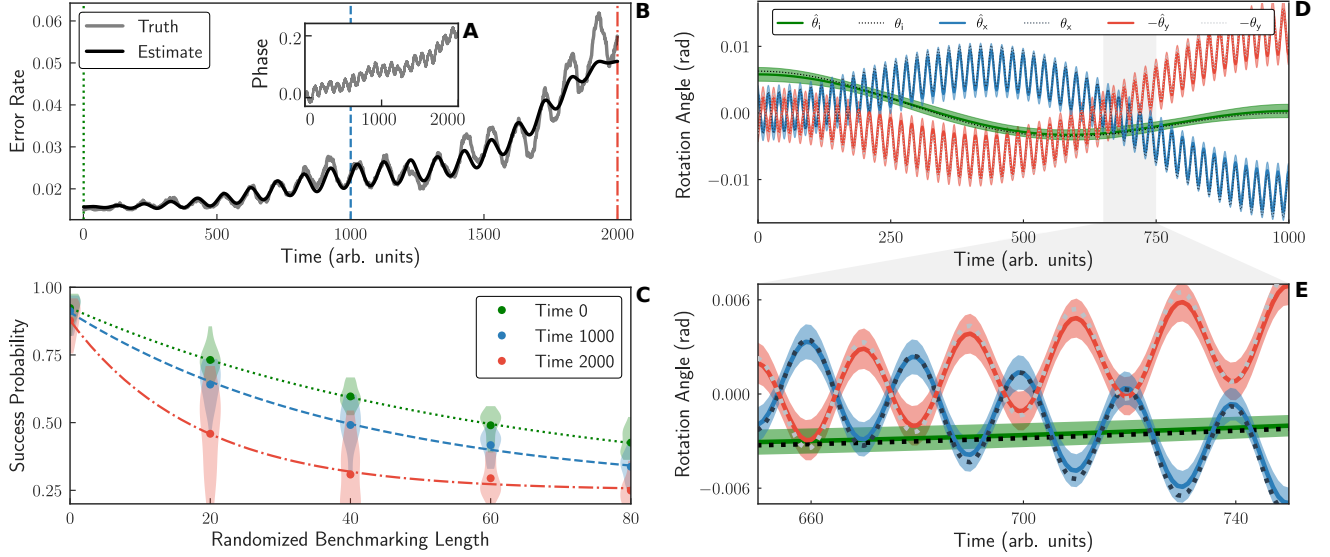


FIG. 2. **Time-resolved randomized benchmarking & tomography on simulated data.** **A-C.** Time-resolved RB on simulated data for gates with time-dependent phase errors. **A.** The simulated phase error over time. **B.** The RB error rate ( $r$ ) versus time and an estimate obtained from simulated data. **C.** Estimated instantaneous average-over-circuits (points) and per-circuit (distributions) success probabilities at each circuit length, and fits to an exponential (curves), for the three times denoted in B. Each instantaneous estimate of  $r$  is a rescaling of the decay rate of the exponential fit at that time. **D-E.** Time-resolved GST on simulated data, for three gates  $G_i$ ,  $G_x$  and  $G_y$  that are subject to time-dependent coherent errors around the  $\hat{z}$ ,  $\hat{x}$  and  $\hat{y}$  axes, respectively, by angles  $\theta_i$ ,  $\theta_x$  and  $\theta_y$ . The estimates of these rotation angles (denoted  $\hat{\theta}_i$ ,  $\hat{\theta}_x$  and  $\hat{\theta}_y$ ) closely track the true values. The shaded areas are  $2\sigma$  confidence regions.

resolved parameterized model  $p(t) = \alpha_0 + \sum_k \alpha_k f_k(t)$ , where  $f_k(t)$  is the  $k^{\text{th}}$  basis function of the Fourier transform (which is real-valued, due to our choice of transformation), the summation is over those frequencies that have been found to be components in the true  $p(t)$  using hypothesis testing, and the  $\alpha_k$  are parameters constrained only so that each  $p(t)$  is a valid probability. We can then fit this model to the clickstream for the corresponding circuit, using any standard data fitting routine, *e.g.*, maximum likelihood estimation.

Estimates of the time-resolved probabilities for the Ramsey experiment are shown in Fig. 1C (unbroken lines). Probability traces are sufficient for heuristic reasoning about the type and size of the errors, and this is often adequate for practical debugging purpose. For example, these probability trajectories strongly suggest that the qubit detuning is slowly drifting. To go beyond this sort of heuristic reasoning, we can implement rigorous time-resolved parameter estimation.

**Time-resolved benchmarking & tomography.** The techniques presented above lay a foundation for constructing time-resolved benchmarking and tomography methods, such as time-resolved estimation of gate error rates, rotation angles, or process matrices. We introduce two complementary approaches for such time-resolved characterization, which we refer to as *non-intrusive* and *intrusive*. The non-intrusive approach is to simply re-

place bulk counts data with instantaneous probability estimates in existing benchmarking/tomography analyses (step 4, Fig 1A). This approach is non-intrusive because it can be implemented without modifications to existing characterization analysis codes. It is particularly well-suited to time-resolved randomized benchmarking (RB), as it maintains the speed and simplicity of RB. The intrusive approach, on the other hand, builds an explicitly time-resolved model and fits the parameters of that model to the time-series data. This has the potential to be more accurate, but it can require substantial modifications to analysis code to upgrade an extant protocol. The intrusive and non-intrusive approaches are both sufficiently general to add time resolution to any benchmarking or tomography protocol.

All standard characterization protocols, including all forms of tomography [7–10] and randomized benchmarking (RB) [12–19], are founded on some time-*independent* parameterized model that describes the outcome probabilities for the circuits in the experiment, or a coarse-graining of them (*e.g.*, mean survival probabilities in RB). When analyzing data from these experiments, the counts data from these circuits are fed into an analysis tool that estimates the model parameters,  $\{\alpha_i\}$ . To upgrade such a protocol using the non-intrusive method, we: (i) use the spectral analysis tools above to construct time-resolved estimates of the probabilities; (ii) for a given time,  $t_j$ , input the estimated probabilities directly into



the analysis tool in place of frequencies; (iii) recover an estimate of the model parameters,  $\{\alpha_i(t_i)\}$  at that time; and (iv) repeat for all times of interest  $\{t_j\}$ . This non-intrusive approach is simple, but statistically *ad hoc*.

The intrusive approach permits statistical rigor at the cost of a more complex analysis. It consists of (i) selecting an appropriate *time-resolved* model for the protocol and (ii) fitting that model to the time-series data (steps 5a-5b, Fig. 1A). In the model selection step, we expand each model parameter  $\alpha$  into a sum of Fourier components:  $\alpha \rightarrow \alpha_0 + \sum_{\omega} \alpha_{\omega} f_{\omega}(t)$ , where the  $\alpha_{\omega}$  are real-valued amplitude, and the summation is over some set of non-zero frequencies. This set of frequencies can vary from one parameter to another, and may be empty if the parameter in question appears to be constant. To choose these expansions we need to understand how any drift frequencies in the model parameters would manifest in the circuit probability trajectories, and so, in turn, the data. This can be ascertained by deriving the sensitivities to the model parameters of each circuit in the experiment. Comparing these sensitivities to the detected frequencies facilitates a principled selection of the model parameter expansions.

To demonstrate the intrusive approach, we return to the Ramsey experiment. The standard time-independent Ramsey model is that the probability to output 1 from a Ramsey circuit with a wait time of  $lt_w$  is  $p_l = A + B \exp(-l/l_0) \sin(2\pi lt_w \Omega)$ , where  $\Omega$  is the detuning between the qubit and the control field,  $1/l_0$  is the rate of decoherence per idle, and  $A, B \approx 1/2$  account for any state preparation and measurement errors. In our Ramsey experiment, the probability trace estimates shown in Fig. 1C suggest strongly that the state preparation, measurement and decoherence error rates are approximately time-independent, as the contrast is constant over time. So we select a time-resolved model that expands only  $\Omega$  into a time-dependent summation:

$$p_l(t) = A + B \exp(-l/l_0) \sin(2\pi lt_w \Omega(t)), \quad (1)$$

where  $\Omega(t) = \alpha_0 + \sum_{\omega} \alpha_{\omega} f_{\omega}(t)$ . To select the set of frequencies in the summation, we observe that, for small  $l$ , the circuit probabilities depend approximately linearly on  $\Omega$  (e.g., expand Eq. (1) around  $lt_w \Omega(t) \approx 0$ ). Therefore, the oscillation frequencies in the model parameters necessarily appear in the circuit probabilities. So we include in our expansion of  $\Omega$  all 13 frequencies detected in the circuit probabilities (i.e., all the frequencies with power above the threshold in Fig. 1C). The circuit probabilities will also contain sums, differences and harmonics of the frequencies in the true  $\Omega$ , so this frequency selection strategy *could* result in erroneously including some of these harmonics in our model. We check for this using standard information-theoretic criteria [51], and then discard any frequencies that should not be in the model. This avoids over-fitting the data. Further details on this model selection, as applied to a generic time-independent

model as well as specifically to this Ramsey model, are provided in the Methods. Once the model is selected, we have a time-resolved parameterized model that we can directly fit to the time-series data, using, e.g., maximum likelihood estimation.

Fig. 1E shows the estimated qubit detuning  $\Omega(t)$  over time, revealing that it varies slowly between approximately  $-0.5$  Hz and  $0.5$  Hz. Strikingly, the detuning is correlated with an ancillary measurement of the ambient laboratory temperature, which fluctuates by approximately  $1.5^\circ\text{C}$  over the course of the experiment. This suggests that temperature fluctuations are causing the drift in the qubit detuning. The detuning has been estimated to high precision, as highlighted by the  $2\sigma$  confidence regions in Fig. 1E. As with all standard confidence regions, these are “in-model” uncertainties, i.e., they do not account for any inadequacies in the model selection. However, we can confirm that the estimated detuning is reasonably consistent with the data by comparing the  $p_l(t)$  predicted by the estimated model (dotted lines, Fig. 1D) with the model-independent probability estimates obtained earlier (unbroken lines, Fig. 1D). These probabilities are in close agreement.

**Demonstration on simulated data.** RB and gate set tomography (GST) are two of the most popular methods for characterizing a QIP [7–10, 12–14]. Both methods are robust to state preparation and measurement errors; RB is fast and simple, whereas GST provides detailed diagnostic information about the types of errors afflicting the QIP. We now demonstrate time-resolved RB and GST on simulated data, using the general methodology introduced above. Full details on how we apply our techniques to RB and GST can be found in the Methods.

We simulated the collection of time-series data from 100 randomly sampled RB circuits [12–14] on two qubits, rastered 2000 times. The error model consisted of 1% depolarization per qubit per gate and a coherent phase error that varies stochastically over time (details in the Methods). A typical phase error versus time is shown in Fig. 2A. The general instability analysis was implemented on this simulated data, after converting the 4-outcome data to the standard “success”/“fail” format of RB. This analysis yielded a time-dependent success probability for each circuit. Following our non-intrusive framework, instantaneous success probabilities at each time of interest were then fed into the standard RB data analysis – i.e., exponential curve fitting – as shown for three times in Fig. 2C. The instantaneous RB error rate estimate is then (up to a constant) the decay rate of the fitted exponential at that time. The resultant time-resolved RB error rate is shown in Fig. 2B. It closely tracks the true error rate.

GST is a method for high-precision tomographic reconstruction of a set of time-independent gates, state preparations and measurements [7–10]. We consider GST on

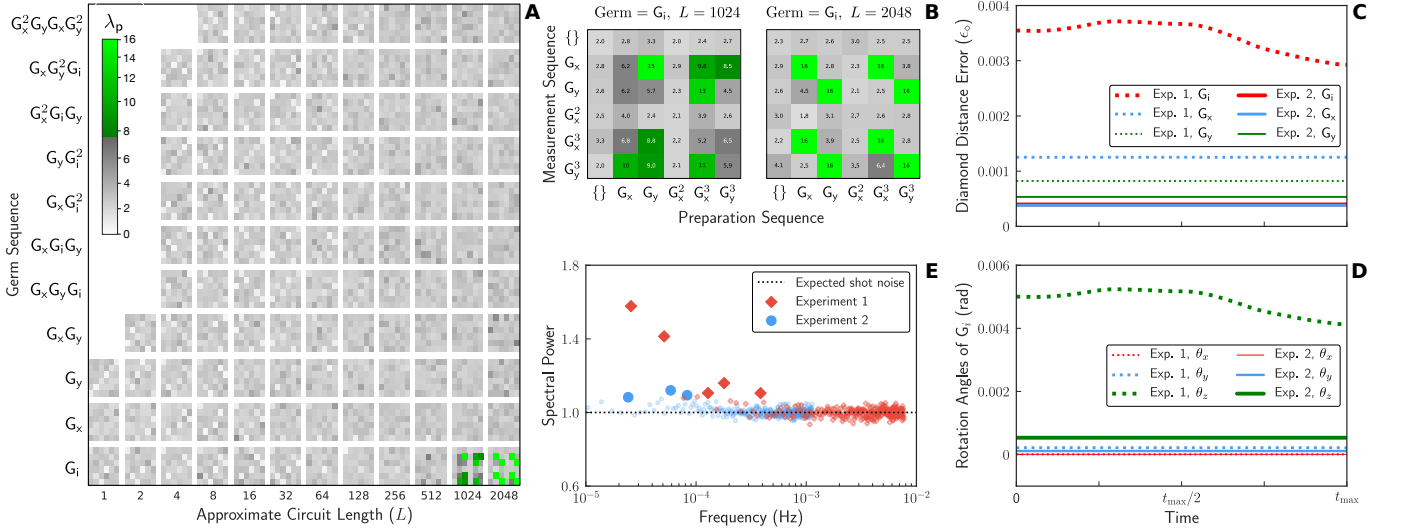


FIG. 3. **Measuring qubit stability using time-resolved GST.** The results of two time-resolved GST experiments – using the gates  $G_i$ ,  $G_x$  and  $G_y$  – with adjustments made after the first experiment aimed at stabilizing the qubit. **A-B.** The evidence for instability in each circuit in the first experiment, quantified by  $\lambda_p$  (see main text). A pixel is colored when  $\lambda_p$  is large enough to be statistically significant, otherwise it is greyscale. Each circuit consists of repeating a *germ* sequence  $l$  times in between six initialization and pre-measurement sequences. The data is arranged by germ and approximate circuit length  $L$ , and then separated into the  $6 \times 6$  different preparation and measurement sequence pairs, as shown on the axes of B (“{” denotes the null sequence). Only long circuits containing repeated applications of  $G_i$  exhibit evidence of drift. In the second experiment none of the  $\lambda_p$  are statistically significant (data not shown). **C-D.** The result of time-resolved tomographic reconstructions of the gates in each experiment, summarized by the diamond distance error of each gate, and the decomposition of the coherent errors in the idle gate  $G_i$  into rotation angles around  $\hat{x}$ ,  $\hat{y}$  and  $\hat{z}$ , over the duration of each experiment ( $t_{\max} \approx 8$  hours and  $t_{\max} \approx 2.5$  days for the first and second experiment, respectively). **E.** The power spectrum for each experiment obtained by averaging the individual power spectra for the different circuits, with filled points denoting power above the 5% significance thresholds (not shown).

three gates  $G_x$ ,  $G_y$ , and  $G_i$  – where  $G_{x/y}$  are  $\pi/2$  rotations around the  $\hat{x}/\hat{y}$  axes and  $G_i$  is the idle gate – alongside the standard  $\hat{z}$ -axis preparation and measurement. The GST circuits have the form  $S_{\text{prep}} S_{\text{germ}}^l S_{\text{meas}}$  (all circuits are written in operation order, *i.e.*, the operations are applied from left to right). In this circuit:  $S_{\text{prep}}$  and  $S_{\text{meas}}$  are each one of six short sequences chosen to generate tomographically complete state preparations and measurements;  $S_{\text{germ}}$  is one of twelve short *germ* sequences, chosen so that powers (repetitions) of these germs amplify all coherent, stochastic and amplitude-damping errors;  $l$  runs over an approximately logarithmically spaced set of integers, given by  $l = \lfloor L/|S_{\text{germ}}| \rfloor$  where  $|S_{\text{germ}}|$  is the length of the germ and  $L = 2^0, 2^1, 2^2, \dots, L_{\max}$  for some maximum germ power  $L_{\max}$ .

We simulated collecting data from 1000 rasters through these GST circuits (with  $L_{\max} = 128$ ). The error model consisted of 0.1% depolarization on each gate. Additionally,  $G_x$  and  $G_y$  are further subject to over/under-rotation errors that oscillate both quickly and slowly, while  $G_i$  is further subject to slowly varying  $\hat{z}$ -axis coherent errors (details in the Methods). The general instability analysis was implemented on this simulated data, the results were used to select a time-resolved model for the gates, and this model was then fit to the time-series data us-

ing maximum likelihood estimation (*i.e.*, this is the intrusive approach to time-resolved GST). The resulting time-resolved estimates of the gate rotation angles are shown in Fig. 2D-E. The estimates closely track the true values.

**Demonstration on experimental data.** Having verified that our methods are compatible with data from GST circuits, we now demonstrate time-resolved GST on two sets of experimental data, using the three gates  $G_x$ ,  $G_y$  and  $G_i$ . These experiments comprehensively quantify the stability of our  $^{171}\text{Yb}^+$  qubit, because the GST circuits are tomographically complete *and* they amplify all standard types of error in the gates. The  $G_x$  and  $G_y$  gates were implemented with BB1 compensated pulses [52, 53], and  $G_i$  was implemented with a dynamical decoupling  $X_\pi Y_\pi X_\pi Y_\pi$  sequence [54], where  $X_\pi$  and  $Y_\pi$  represent  $\pi$  pulses around the  $\hat{x}$  and  $\hat{y}$  axes. The first round of data collection included the GST circuits to a maximum germ power of  $L_{\max} = 2048$  (resulting in 3889 circuits). These circuits were rastered 300 times over approximately 5.5 hours.

Fig. 3A-B summarizes the results of our general instability assessment on this data, using a representation that is tailored to GST circuits. Each pixel in this plot corre-

sponds to a single circuit, and summarizes the evidence for instability by  $\lambda_p = -\log_{10}(p)$  where  $p$  is the  $p$ -value of the largest power in the spectrum for that circuit ( $\lambda_p$  is 5% significant when it is above the multi-test adjusted threshold  $\lambda_{p,\text{threshold}} \approx 7$ ). The only circuits that displayed detectable instability are those that contain many sequential applications of  $G_i$ . Fig. 3B further narrows this down to generalized Ramsey circuits, whereby the qubit is prepared on the equator of the Bloch sphere, active idle gates are applied, and then the qubit is measured on the equator of the Bloch sphere. These circuits amplify erroneous  $\hat{z}$ -axis rotations in  $G_i$ . Other GST circuits amplify all other possible errors in  $G_i$  (and  $G_x$  and  $G_y$ ), but none of those circuits exhibit detectable drift. So it must be the angle of these  $\hat{z}$ -axis rotations that is varying over the course of the experiment.

The instability in the  $G_i$  gate can be quantified by implementing time-resolved GST, with the  $\hat{z}$ -axis error in  $G_i$  expanded into a summation of Fourier coefficients. The results are summarized in Fig. 3C-D (dotted lines). Fig. 3C shows the *diamond distance error rate* ( $\epsilon_o$ ) [55] in the three gates over time, highlighting that  $G_i$  is the worst performing gate, and that the error rate of  $G_i$  drifts substantially over the course of the experiment. The gate infidelities are an order of magnitude smaller (see the Methods). Fig. 3D shows the coherent component of the  $G_i$  gate over time, resolved into rotation angles  $\theta_x$ ,  $\theta_y$  and  $\theta_z$  around the three Bloch sphere axes  $\hat{x}$ ,  $\hat{y}$  and  $\hat{z}$ . The varying  $\hat{z}$ -axis component is the dominant source of error. The  $G_i$  gate is an active  $X_\pi Y_\pi X_\pi Y_\pi$  pulse sequence, so the  $\hat{z}$ -axis rotation in  $G_i$  is sensitive to over/under rotation errors in these pulses at 2<sup>nd</sup> order, whereas  $G_x$  and  $G_y$  are only sensitive to these errors at 4<sup>th</sup> order (as they are BB1 pulse sequences). This suggests that the drifting  $\hat{z}$ -axis rotation error could be caused by drift in the amplitude of the microwave pulses.

This first round of experiments revealed some instability, so changes were made to the experimental setup aiming to mitigate drift and improve qubit performance. This included the addition of periodic recalibration of the pulses (detailed in the Methods). We then repeated these GST experiment, but – to increase sensitivity to any instability – we collected more data, over a longer time period, and included longer circuits. We ran the GST circuits out to a maximum germ power of  $L_{\text{max}} = 16384$ , rastering 328 times through this set of 5041 circuits over approximately 2.5 days. Repeating the above analysis, we found that none of the  $\lambda_p$  were statistically significant, *i.e.*, no instability was detected in *any* circuit, including circuits containing over  $10^5$  sequential  $G_i$  gates. Again, we performed time-resolved GST. Since no time dependence was detected, this reduces to standard *time-independent* GST. The results are summarized in Fig. 3C-D (unbroken lines). The gate error rates have been substantially suppressed, and the  $\hat{z}$ -axis coherent error in  $G_i$  reduced and stabilized.

No individual circuit exhibits signs of drift in this second GST experiment, but we can also perform a collective test for instability on the clickstreams from all the circuits. In particular, we can average the per-circuit power spectra, and look for statistically significant peaks in this single spectrum. This suppresses the shot noise inherent in each individual clickstream, so it can reveal low-power drift that would otherwise be hidden in the noise. This average spectrum is shown for both experiments in Fig. 3E. The power at low frequencies decreases substantially from the first to the second experiment, further demonstrating that our drift mitigation is stabilizing the qubit. However, there is power above the 5% significance threshold for both experiments. So there is still some residual instability after the experimental improvements. This residual drift is no longer a significant source of errors, as demonstrated by the low and stable error rates shown in Fig. 3C.

## DISCUSSION

Reliable, useful quantum computation demands stable hardware. But current standards for characterizing QIPs *assume* stability – they cannot verify that a QIP is stable, nor can they quantify any instabilities. This is becoming a critical concern as stable sources of errors are steadily reduced. For example, drift significantly impacted the recent tomographic experiments of Wan *et al.* [26] but this was only verified using a complicated and arguably rather *ad hoc* analysis. In this article we have introduced a general, flexible, and powerful methodology for diagnosing instabilities in a QIP. We have applied these methods to a trapped-ion qubit, demonstrating both time-resolved phase estimation and time-resolved tomographic reconstructions of logic gates. Using these tools, we were able to identify the most unstable gate, and then confirm that periodic recalibration stabilized the qubit to an extent that drift is no longer a significant source of error in the qubit.

The methods we have proposed and demonstrated are widely-applicable, platform-independent, and fast: the core techniques are applicable to data from *any* set of quantum circuits as long as it is recorded as a time series, and they are limited in speed only by the fast Fourier transform. These techniques are even applicable outside of the context of quantum computing – *e.g.*, they could be used for time-resolved quantum sensing. We have incorporated these tools into an open-source software package [56], making it a simple matter to check any time-series QIP data for signs of instability. Because of the disastrous impact of drift on characterization protocols [20–26], its largely unknown impact on QIP applications, and the minimal overhead required to implement our methods, we expect that this analysis will be broadly and quickly adopted.

## METHODS

**Experiment details.** We trap a single  $^{171}\text{Yb}^+$  ion approximately  $34\mu\text{m}$  above a Sandia multi-layer surface ion trap with integrated microwave antennae, shown in Fig. 4. The radial trapping potential is formed with 170 V of rf-drive at 88 MHz; the axial field is generated by up to 2 V on the segmented dc control electrodes. This yields secular trap frequencies of 0.7 MHz, 5 MHz, and 5.5 MHz for the axial and radial modes, respectively. An electromagnetic coil aligned with its axis perpendicular to the trap surface creates the quantization field of approximately 5 G at the ion. The field magnitude is calibrated using the qubit transition frequency, which has a second-order dependence on the magnetic field of  $f = 12.642812118\text{ GHz} + 310.8B^2\text{ Hz}$ , where  $B$  is the externally applied magnetic field in Gauss [57]. The qubit is encoded in the hyperfine clock states of the  $^2\text{S}_{1/2}$  ground state of  $^{171}\text{Yb}^+$ , with logical 0 and 1 defined as  $|0\rangle \equiv |F=0, m_F=0\rangle$  and  $|1\rangle \equiv |F=1, m_F=0\rangle$ .

Each run of a quantum circuit consists of the same four steps: cooling the ion, preparing the input state, performing the gates, and then measuring the ion. First, using an adaptive length Doppler cooling scheme, we verify the presence of the ion. The ion is Doppler cooled for 1 ms, during which fluorescence events are detected and counted. If the number of detected photons is above a threshold – set to approximately 85% of the average fluorescence observed for a cooled ion – Doppler cooling is complete, otherwise, the cooling is repeated. If the threshold is not reached after 300 repetitions, the experiment is halted to load a new ion. This procedure ensures that an ion is present in the trap and that it has approximately the same temperature for each run. After cooling and verifying the presence of the ion, it is prepared in the  $|F=0, m_F=0\rangle$  ground state (logical 0) using an optical pumping pulse [58]. All active gates in the circuit are implemented by directly driving the 12.6428 GHz hyperfine qubit transition, using a near-field antenna integrated into the trap (see Fig. 4). The methods used for generating the microwave radiation are discussed in Ref. [7]. A standard state fluorescence technique [58] is used to measure the final state of the qubit.

In the Results we presented three experiments: one experiment consisting of collecting time-series data from Ramsey circuits (see Fig. 1), and two experiments consisting of collecting time-series data from GST circuits (see Fig. 3). Both sets of circuits contain  $G_x$  and  $G_y$  gates, which are  $\pi/2$  rotations around the  $\hat{x}$ - and  $\hat{y}$ -axes, implemented using BB1 pulse sequences [52, 53]. The Ramsey circuits also contain  $G_{\text{wait}}$  gates, which are passive idles. The GST circuits also contain  $G_i$  gates, which are active idles implemented using a second-order compensation sequence:  $G_i = X_\pi Y_\pi X_\pi Y_\pi$ , where  $X_\pi$  and  $Y_\pi$  denote  $\pi$  rotations about the  $\hat{x}$ - and  $\hat{y}$ -axis, respectively [54]. The passive idle gate  $G_{\text{wait}}$  consists of waiting for the same length of time as taken to implement a  $G_i$  gate. In the Ramsey experiment, this is  $410.4\mu\text{s}$ . The time taken for each active gate was changed between the three experiments, as the Rabi frequency of the microwave pulses was altered to reduce sensitivity to sources of drift. To maintain a constant power on the microwave amplifier, and reduce the errors from finite on/off times, all sequences of active gates are performed gapless (so in the GST experiments, every circuit is implemented entirely gapless). This means that we transition from one pulse to the next by adjusting the phase

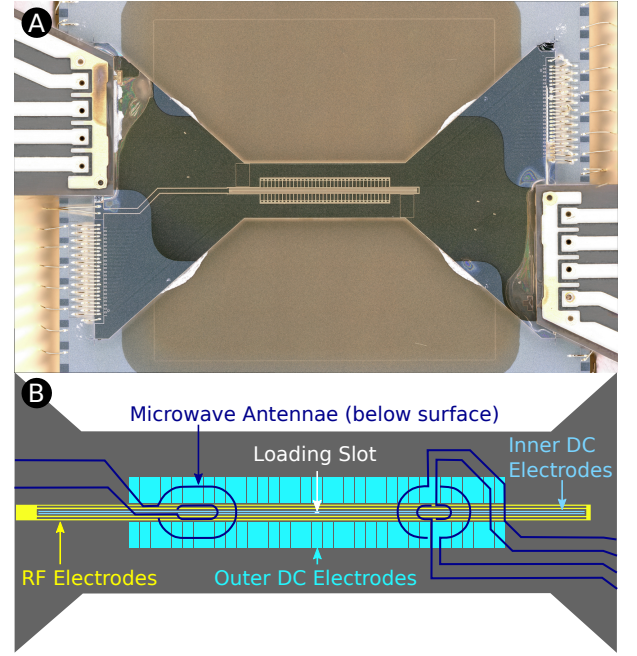


**FIG. 4. The Sandia ion trap.** A  $^{171}\text{Yb}^+$  ion is loaded in the center of the trap, by photo-ionizing neutral ytterbium vapor introduced through the loading slot in the device. It is then shuttled to the center of the microwave antenna on the left. **A.** Flex cable microwave waveguides (upper left and lower right) are solder-die attached to the trap die to circumvent the trap package. This limits unintended impedance changes and losses, and optimizes the microwave power reaching the antenna. **B.** A schematic of the trap showing the antennae locations with respect to the dc control and rf electrodes. The leads for the microwave antennae attach directly to the flex cable waveguides. The antennae are located on the lowest metal layer underneath the trap electrodes. While the generated magnetic field is attenuated by the metal layers above it, the gaps between electrodes make this design viable and the magnetic field above the trap is about half of the field strength generated if the antennae would not be covered by trap electrodes.

of the microwave signal without changing the amplitude of the microwave radiation.

The Ramsey experiment consists of circuits composed of a  $G_x$  gate, followed by  $l$   $G_{\text{wait}}$  gates with  $l = 2^0, 2^1, \dots, 2^{13}$ , and ending with a  $G_y$  gate (see Fig. 1B). The Rabi frequency was 10 kHz (but as there are only two active gates in each circuit, the exact Rabi frequency is of minimal relevance when interpreting this data). In these experiments, the ion was situated at the center of the trap, above the loading slot. In Fig. 1E we compare the drift that we estimate in the qubit detuning with ambient laboratory temperature. This was measured by placing a temperature probe on the wall, near the apparatus, to monitor the air temperature.

In both GST experiments the ion was located above the center of the left microwave antenna (see Fig. 4). In the first set of GST experiments the Rabi frequency was 119 kHz. This results in the  $G_i$  and  $G_{x/y}$  gates taking approximately  $17\mu\text{s}$  and  $19\mu\text{s}$ , respectively. Changing the phase in the analog output signal takes a finite time of about 5 ns. As the pulse sequences



are performed gapless, this causes errors, and these errors are larger for shorter  $\pi$ -pulse times. To reduce this error, in this second GST experiment the Rabi frequency was decreased to 74 kHz. We also incorporated two forms of active drift control. Fluctuations in the power output of the microwave amplifier are a known problem – and a possible cause for the drift observed in  $G_i$  in the first GST experiment – so we periodically calibrate the  $\pi$ -pulse time to compensate for these changes. After every 4<sup>th</sup> circuit, a calibration circuit consisting of a  $10.5\pi$  pulse was performed. If the outcome is 0 (resp., 1) then 1.25 ns is added to (resp., subtracted from) the  $\pi$ -time. The  $\pi$ -time is rounded to an integer multiple of 20 ns, so that only consistently bright or dark measurements result in changes of the pulse time. To calibrate the frequency, after every 16<sup>th</sup> circuit a calibration circuit consisting of a  $G_x$  gate, a 10 ms wait and a  $G_y$  gate was performed. If the outcome is 0 (resp., 1) 10 mHz is added to (resp., subtracted from) the applied microwave frequency.

**The power spectra.** Here we detail how the data is transformed into power spectra, *i.e.*, we specify the method of step 1 in the flowchart of Fig. 1A. The power spectra are calculated by applying a Fourier-like transform  $F$  to rescaled data. Throughout this article, all data analysis uses the Type-II discrete cosine transform (DCT), with an orthogonal normalization, given by

$$F_{\omega i} = \sqrt{\frac{2^{1-\delta_{\omega,0}}}{N}} \cos\left(\frac{\omega\pi}{N} \left(i + \frac{1}{2}\right)\right), \quad (2)$$

where  $\omega, i = 0, \dots, N-1$  [59, 60]. The Type-II DCT typically results in a sparser representation of signals with differing values at the boundaries than many of the alternative Fourier-like transforms [59, 60]. Signals of this sort are typical in our problem, and so this is our motivation for using this transform.

Although all our data analysis uses the Type-II DCT, our methods – and much of the supporting theory – are all directly applicable for any transform matrix  $F$  that satisfies the following criteria: (i)  $F$  is orthogonal, (ii) every matrix element of  $F$  satisfies  $F_{\omega i}^2 \leq b_F/N$  for a small constant  $b_F$ , and (iii) the top row of  $F$  is proportional to the vector of all ones. This includes, *e.g.*, sine transforms, other cosine transforms, and the Walsh-Hadamard transform [59–61] (with appropriate normalizations). Note that the discrete Fourier transform does *not* satisfy these requirements (with an appropriate normalization it is unitary, but not orthogonal). However, the methods described here are compatible with the discrete Fourier transform as long as some minor adjustments are made to guarantee that, *e.g.*, the probability trace estimates are real. Throughout the following theory, we refer to the indices of the  $F$ -domain vector as *frequencies*, but note that (i) when we report frequencies for experimental data these indices have been converted to Hertz, and (ii) for a generic transformation an index should only be interpreted as indicating the corresponding basis function of  $F$ , and may or may not constitute a frequency.

As discussed in the Results, the motivation for using spectral analysis is that many physically plausible  $p(t)$  are sparse in the frequency domain, but note that the relevant quantity to the data analysis is the discrete-time probability trajectory  $\vec{p}$ , where  $p_i = p(t_i)$  and  $t_i$  is the  $i^{\text{th}}$  data collection time for the circuit in question. Moreover, as we are concerned with deviations from time-independence, it is the *signal* vector  $\vec{s} = \vec{p} - \bar{p}$

that is of most relevance, where  $\bar{v}$  denotes the mean of the vector  $\vec{v}$  and  $\vec{v} - \bar{v}$  is shorthand for  $(v_0 - \bar{v}, v_1 - \bar{v}, \dots)^T$ . It is sparsity of  $\vec{s}$  that is important for our data analysis. Sparsity in the frequency domain of the continuous-time probability  $p(t)$  implies that  $\vec{s}$  is a sparse vector if: (i) a sensible choice is made for the transformation  $F$ , (ii) the number of sample times  $N$  is sufficiently high, and (iii) the sample times  $t_0, t_1, t_2, \dots, t_{N-1}$  for the circuit in question are spaced reasonably uniformly.

All the experiments and simulations herein consist of rastering through a set of circuits, and so the time between sequential runs of a circuit is exactly constant (and the same for all the circuits) in an *idealized* experiment. Violations of this ideal are unavoidable, but if they are small – as they are in our experiments – they only mildly degrade the effectiveness of our techniques. This can be understood by noting that small perturbations on equally-spaced times (or a small number of erroneously long time-steps of any size) will only slightly reduce the sparsity of  $\vec{s}$ , for generic Fourier-sparse  $p(t)$ . Large deviations from the equally-spaced-times ideal can substantially degrade the methods we presented in the Results (although this will *not* cause instability to be spuriously detected). In this case, we can instead generate power spectra using a technique that explicitly takes into account the sample times. One such option is the *floating-mean Lomb-Scargle periodogram* [62, 63], and all our methods can be adapted to this spectral analysis technique. As there are a range of technical differences in this case, and this method is not needed to analyze our experimental data, we do not include the details here.

Before transforming a clickstream to the frequency domain, we first subtract its mean and divide by its variance. This simplifies the statistics of the power spectrum, but the spectrum is not well-defined if the clickstream consists of only 0s or only 1s. So we define the frequency-domain amplitudes by:

$$\tilde{z} = \begin{cases} \frac{F(\vec{x} - \bar{x})}{\sqrt{\bar{x}(1-\bar{x})}} & \text{if } 0 < \bar{x} < 1, \\ (0, 1, 1, \dots) & \text{else,} \end{cases} \quad (3)$$

where, as above,  $\vec{x} - \bar{x} \equiv (x_0 - \bar{x}, x_1 - \bar{x}, \dots)^T$ . The power at frequency  $\omega$  is then given by  $|\tilde{z}_\omega|^2$ . This convention for the constant clickstream case is convenient, and it roughly corresponds to the  $N \rightarrow \infty$  limit of  $\tilde{z}$  for a clickstream containing a single 1 or 0 (the correspondence is not precise, because the spectrum of a delta function is not completely flat for a general transform  $F$ ).

**Statistical hypothesis testing.** All of the methods presented herein are built upon *statistical hypothesis testing* [49, 50]. We now review the relevant aspects of this field and formulate our hypothesis testing problem. Consider some set of random variables  $\{A_1, A_2, \dots\}$  with a joint distribution that is parameterized by  $\theta \in \mathcal{H}$  for some space  $\mathcal{H}$ . A statistical hypothesis is the conjecture that  $\theta \in \mathcal{H}_0 \subset \mathcal{H}$ . In this article, data consists of a clickstream of  $N$  bits for each of  $C \geq 1$  circuits. Generalizing the notation used in the Results so that we explicitly denote the circuit index, let  $x_{c,i}$  be the bit output by the  $i^{\text{th}}$  repetition of the  $c^{\text{th}}$  circuit, and denote the corresponding Bernoulli random variable from which that datum is drawn by  $X_{c,i}$ . The set of random variables about which we state statistical hypotheses is  $\{X_{c,i}\}$ . The random variable  $X_{c,i}$  has some unknown probability  $p_{c,i}$  of taking the value 1, so the set of random variables  $\{X_{c,i}\}$  is parameterized by the parameter space  $\mathcal{H} = \{p_{c,i} \in [0, 1]\}$ .

Statistical hypothesis testing starts from some set of *null hypotheses*  $\{\mathcal{H}_{0,i}\}$  and uses statistical hypothesis tests on data drawn from the random variables to attempt to reject one or more of these null hypotheses (and/or intersections of these null hypotheses). Our methods look for evidence that  $|\tilde{p}_{\omega,c}| > 0$  at each non-zero frequency  $\omega$  and for each circuit. This is formalized by the set of null hypotheses  $\{\mathcal{H}_{0,c,\omega}\}$  where  $\mathcal{H}_{0,c,\omega}$  is the conjecture that  $\tilde{p}_{c,\omega} = 0$ , with  $\omega = 1, 2, \dots, N-1$  and  $c = 1, 2, \dots, C$ . For our purposes, testing a null hypothesis consists of the following four steps: (i) pick a significance level  $\alpha \in (0, 1)$ , with  $\alpha = 5\%$  a common choice; (ii) select a *test statistic*  $\Lambda$ , which is a function from data to  $\mathbb{R}$ ; (iii) find a threshold such that the probability of observing  $\Lambda$  larger than this threshold if the null hypothesis is true is at most  $\alpha$ ; (iv) collect data, evaluate  $\Lambda$ , and reject the null hypothesis if and only if  $\Lambda$  is larger than the threshold. This procedure guarantees that the null hypothesis is falsely rejected with probability at most  $\alpha$ . Our test statistic for testing the null hypothesis  $\mathcal{H}_{0,c,\omega}$  is simply the power of the normalized data at the frequency  $\omega$ , i.e.,  $|\tilde{z}_{c,\omega}|^2$ .

Implementing multiple hypothesis tests that use the above procedure will typically cause the probability of falsely rejecting at least one null hypothesis – the *family-wise error rate* (FWER) – to increase quickly with the number of tests (for  $T$  tests  $\text{FWER} \leq T\alpha$ ). The standard approach when implementing multiple tests is to adapt the testing procedure to, at a minimum, maintain *weak control* of the FWER. This means that, if all the null hypotheses are true, then for some pre-specified *global significance*  $\alpha$  the probability of falsely rejecting one or more null hypotheses is at most  $\alpha$ . It is common to choose a testing procedure that also maintains *strong control* of the FWER. This means that the probability of falsely rejecting one or more true null hypotheses is at most  $\alpha$  and this holds even if one or more of the null hypotheses are false. We seek to maintain strong control of the FWER, so that whenever we reject  $\mathcal{H}_{0,c,\omega}$  we can be  $(1 - \alpha)$  confident that  $\omega$  is indeed a frequency in  $\tilde{p}_c$ .

Strong control of the FWER at a global significance of  $\alpha$  can be maintained by implementing the  $i^{\text{th}}$  of  $T$  tests at a *local significance* of  $\alpha w_i$  for any  $w_i \geq 0$  satisfying  $\sum_i w_i = 1$ . This is known as the *Bonferroni correction* [49, 50]. The Bonferroni correction can be conservative; there are other methods for maintaining strong control of the FWER that are more powerful than the Bonferroni correction, such as the Holms procedure [49, 50]. Moreover, strong control of the FWER is not the only way to ensure “confidence” in the results – e.g., we could instead choose to control the *false discovery rate*, which is the expected ratio of the number of falsely rejected null hypotheses to the total number of rejected null hypotheses [64]. Variants of our techniques that control the false discovery rate and/or use a different multi-test correction procedure are possible, and essentially involve setting a slightly lower power significance threshold in the analysis.

**Statistics of the power spectra.** Here we derive the distribution of the power spectrum of the data, which is required to explain how we set the power significance threshold. We consider the frequency-domain data  $\tilde{z}_\omega$ , defined in Eq. (3), for an arbitrary non-zero frequency  $\omega$ , and we derive an approximation to the distribution of the corresponding random variable  $\tilde{Z}_\omega$  (we are again dropping the circuit indexing, and we do so whenever convenient without further comment). In the Results we asserted that  $\tilde{Z}_\omega$  is approximately  $\chi_1^2$  distributed whenever the probability trajectory is a constant. This is

a sub-case of what we derive below, but we also study the marginal distribution of  $\tilde{Z}_\omega^2$  when  $\tilde{p}_\omega = 0$  but the probability trajectory is not necessarily constant. We do so in order to be able to claim that we are maintaining *strong* control of the FWER. By itself, the fact that  $\tilde{Z}_\omega^2$  is approximately  $\chi_1^2$  distributed when the probability trajectory is constant can only be used to ensure *weak* control of the FWER.

Let  $\tilde{p}$  be a probability trajectory satisfying  $0 < \tilde{p} < 1$ , and define the time-domain random variables

$$Y_i = \frac{X_i - \tilde{p}}{\sqrt{\tilde{p}(1 - \tilde{p})}}. \quad (4)$$

To convert the frequency-domain random variable  $\tilde{Y}_\omega$  to  $\tilde{Z}_\omega$  we simply replace  $\tilde{p}$  in the definition of  $Y_i$  with the average of the  $X_i$  random variables. As  $\frac{1}{N} \sum_i X_i \approx \tilde{p}$  for  $N \gg 1$ , the distribution of  $\tilde{Z}_\omega$  is closely approximated by the distribution of  $\tilde{Y}_\omega$  in the only regime of interest (i.e., a reasonable length clickstream). Indeed, this is the core motivation for the particular normalization of the data spectrum that we use. So, we now approximate  $\tilde{Z}_\omega$  by  $\tilde{Y}_\omega$ .

The expansion  $\tilde{Y}_\omega = \sum_i F_{\omega i} Y_i$  highlights that  $\tilde{Y}_\omega$  is the sum of  $N$  independent random variables. So a heuristic appeal to the central limit theorem suggests that  $\tilde{Y}_\omega$  is normally distributed. That is,  $\tilde{Y}_\omega$  is approximately  $\mathcal{N}(\mu_\omega, \nu_\omega)$  distributed for large  $N$ , with some mean  $\mu_\omega = \mathbb{E}(\tilde{Y}_\omega)$  and variance  $\nu_\omega = \mathbb{V}(\tilde{Y}_\omega)$ , where  $\mathbb{E}(A)$  and  $\mathbb{V}(A)$  denote the expectation value and variance of the random variable  $A$ , respectively. Later we formally apply the central limit theorem to  $\tilde{Y}_\omega$ , but first we derive formula for the  $\mu_\omega$  and  $\nu_\omega$ . For any non-zero  $\omega$ ,  $\mu_\omega$  is simply a rescaling of the component of the probability trajectory at this frequency:  $\mu_\omega \propto \sum_i \mathbb{E}(F_{\omega i} X_i) = \sum_i F_{\omega i} p_i = \tilde{p}_\omega$ . So if  $\tilde{p}_\omega = 0$  then  $\mu_\omega = 0$ . The variance  $\nu_\omega$  has a more subtle dependence on the probability trajectory. By noting that  $\tilde{Y}_\omega$  is a summation of *independent* Bernoulli random variables multiplied by constants, and by noting that the variance of a Bernoulli random variable with bias  $b$  is  $b(1 - b)$ , we obtain  $\nu_\omega = \frac{1}{\tilde{p}(1 - \tilde{p})} \sum_i F_{\omega i}^2 p_i (1 - p_i)$ . It then follows from the orthogonality of  $F$  that  $\nu_\omega = 1$  when the probability trajectory is constant. Ignoring the approximations made so far, this implies that  $\tilde{Z}_\omega^2$  is  $\chi_1^2$  distributed when the probability trajectory is constant. So calculating significance thresholds using the model that  $\tilde{Z}_\omega^2$  is  $\chi_1^2$  distributed under the null hypothesis will maintain weak control of the FWER.

Using the expansion  $p_i = s_i + \tilde{p}$ , where  $\tilde{s}$  is the zero-mean signal vector, we can rewrite the variance as  $\nu_\omega = 1 + \frac{\Delta_\omega}{\tilde{p}(1 - \tilde{p})}$  where

$$\Delta_\omega = \sum_{i=0}^{N-1} F_{\omega i}^2 (s_i [1 - 2\tilde{p}] - s_i^2). \quad (5)$$

Because  $\sum_i s_i = 0$ , if all the elements of  $F$  satisfy  $F_{\omega i}^2 = 1/N$  then  $\Delta_\omega = -\|\tilde{s}\|_2^2/N$  (this is the case if  $F$  is the Walsh-Hadamard transformation). That is, the variance is upper-bounded by 1, and it decreases in proportion to the signal power per time-step. So the maximum variance over the null hypothesis space of  $\tilde{p}_\omega = 0$  is  $\nu_\omega = 1$ . This means that modeling  $\tilde{Z}_\omega^2$  with a  $\chi_1^2$  distribution is sufficient for strong control of the FWER with power spectra generated using, e.g., the Walsh-Hadamard transformation.

For a general transformation the situation is more complicated. In particular, it is possible to obtain  $\nu_\omega > 1$  for a matrix  $F$  containing elements of magnitude greater than  $1/\sqrt{N}$ . Because all of our data analysis uses the Type-II DCT,

defined in Eq. (2), at this point we specialize to this transformation. In this case, simple algebra can be used to show that

$$\Delta_\omega = \frac{1}{\sqrt{2N}} (\tilde{s}_{2\omega}[1 - 2\bar{p}] - \tilde{q}_{2\omega}) - \frac{\|\tilde{s}\|_2^2}{N}, \quad (6)$$

where  $\tilde{q} = (s_0^2, s_1^2, s_2^2, \dots)$  is the vector of time-domain signal powers vector, and we are allowing the frequency index to extend outside its range as specified in the definition of the DCT. This equation implies that the variance at  $\omega$  is increased by signal power at  $2\omega$  if the oscillations are not centered on  $1/2$ . This can only result in a variance above 1 if the amplitude at  $2\omega$  outweighs the decrease in the variance caused by the total power per time-step in  $\tilde{s}$ . So the variance at  $\omega$  is maximized by a pure-tone probability trajectory oscillating between  $1/2$  and 1 or 0 at a frequency of  $2\omega$ , resulting in the bound  $\nu_\omega \leq 1 + 1/6$ . Therefore the maximal variance over the null hypothesis space of  $\tilde{p}_\omega = 0$  is  $\nu_\omega = 7/6$ . So, ignoring the two approximations made so far, there exists a probability trajectory within the null hypothesis subspace defined by  $\tilde{p}_\omega = 0$  such that  $\tilde{Z}_\omega$  is  $\mathcal{N}(0, 7/6)$  distributed. This implies that calculating significance thresholds using a  $\chi_1^2$  does not strictly provide strong control of the FWER.

We *could* guarantee strong control of the FWER by calculating thresholds using a rescaled  $\chi_1^2$  distribution (or, equivalently, by normalizing the data differently). But we choose not to do this, because for a broad class of probability trajectories  $\nu_\omega \leq 1$  for all  $\omega$ . So accounting for the possibility of  $\nu_\omega > 1$  would result in a significant reduction in test power (*i.e.*, higher significance thresholds) to gain statistical rigor in some edge cases. In our opinion this is not a good tradeoff, and we instead settle for maintaining weak control of the FWER and “almost” maintaining strong control of the FWER. This is true in the sense that although there are some probability trajectories for which the FWER is slightly above the desired value, (i) the increase in the FWER is small, (ii) it can only occur for extremal points in the parameter space, and (iii) it is counteracted by the conservative nature of the Bonferroni correction we use when calculating thresholds from a  $\chi_1^2$  distribution (see later). All further statements about strong control of the FWER should be understood to implicitly contain this minor caveat.

We now prove that the  $N \rightarrow \infty$  limiting distribution of  $(\tilde{Y}_\omega - \mu_\omega)/\sqrt{\nu_\omega}$  is  $\mathcal{N}(0, 1)$ , under a reasonable notion of the limit of a probability trajectory. In particular, we assume that  $\epsilon < \bar{p} < 1 - \epsilon$  and  $\nu_\omega > \tilde{\epsilon}$  for some constants  $\epsilon, \tilde{\epsilon} > 0$  and all  $N$ . The proof will use *Lyapunov’s central limit theorem* [65], which we now state. Let  $\{A_1, A_2, \dots, A_n\}$  be a sequence of independent random variables where  $A_i$  has a finite expected value  $\mu_i$  and variance  $\nu_i$ , and define  $s_n^2 = \sum_i \nu_i$ . Then, if *Lyapunov’s condition*

$$\lim_{n \rightarrow \infty} \frac{1}{s_n^{2+\delta}} \sum_{i=1}^n \mathbb{E} \left[ |A_i - \mu_i|^{2+\delta} \right] = 0, \quad (7)$$

holds for some  $\delta > 0$ , the distribution of  $A = \sum_{i=1}^n (A_i - \mu_i)/s_n$  converges to  $\mathcal{N}(0, 1)$  as  $N \rightarrow \infty$ . The random variable  $\tilde{Y}_\omega$  may be written in the format of this central limit theorem:  $\tilde{Y}_\omega = \sum_i Q_{\omega i}$  where  $Q_{\omega i} = F_{\omega i} Y_i$ , and the expected value and variance of every  $Q_{\omega i}$  is bounded (due to our assumptions). It remains to prove that Lyapunov’s condition holds. We have that  $\mathbb{E} [Q_{\omega i} - \mathbb{E}[Q_{\omega i}]]^3 \leq \mathcal{O}(|F_{\omega i}|^3)$  because  $Q_{\omega i} = F_{\omega i} Y_i$  and the moments of  $Y_i$  are bounded from above by a constant

(as  $\epsilon < \bar{p} < 1 - \epsilon$ ). Therefore

$$\frac{1}{s_n^3} \sum_{i=0}^{N-1} \mathbb{E} [Q_{\omega i} - \mathbb{E}[Q_{\omega i}]]^3 \leq \frac{1}{s_n^3} \sum_{i=0}^{N-1} \mathcal{O}(|F_{\omega i}|^3) = \mathcal{O} \left( \frac{1}{\sqrt{N}} \right),$$

with the equality holding because  $s_n^3 = \nu_\omega^{3/2}$  and  $\nu_\omega > \tilde{\epsilon}$ . So Lyapunov’s condition holds for  $\delta = 1$ .

In addition to performing hypothesis testing on the power spectrum for each circuit, we also test the single power spectrum obtained by averaging over the power spectra for the different circuits, *e.g.*, see Fig. 3E. The power at frequency  $\omega$  in this spectrum is given by  $\tilde{z}_{\text{avg}, \omega}^2 = \frac{1}{C} \sum_c \tilde{z}_{c, \omega}^2$  where  $C$  is the number of circuits. The clickstreams for different circuits are independent, and so the corresponding random variable  $\tilde{Z}_{\text{avg}, \omega}^2$  is the average of independent random variables that are approximately  $\chi_1^2$  distributed under the (intersection) null hypothesis  $\mathcal{H}_{0, \omega} = \cap_c \mathcal{H}_{0, c, \omega}$  that  $\tilde{p}_{c, \omega} = 0$ , for all  $c$ . Therefore  $\tilde{Z}_{\text{avg}, \omega}^2$  is approximately  $\chi_C^2/C$  under this null hypothesis.

**Hypothesis testing of the power spectra.** Here we explain how to calculate the power significance threshold. We argued above that  $\tilde{Z}_{c, \omega}^2$  can be modeled as a  $\chi_1^2$  random variable under the null hypothesis that  $\tilde{p}_{c, \omega} = 0$  (up to minor caveats). So if we are only testing a single circuit  $c$  and frequency  $\omega$ , then the  $\alpha$ -significance power threshold is simply  $\text{CDF}_1^{-1}(1 - \alpha)$ , where  $\text{CDF}_k$  denotes the cumulative distribution function for the  $\chi_k^2$  distribution. However, we test every circuit at every frequency (except  $\omega = 0$ ), and we also test the average power spectrum. To maintain strong control of the FWER with a global significance of  $\alpha$  in this set of  $(N - 1)(C + 1)$  tests, we use a Bonferroni correction. In general, this means setting the local significance of the test on circuit  $c$  at frequency  $\omega$  to  $w_{c, \omega} \alpha$ , and setting the local significance of the test on the average power spectrum at frequency  $\omega$  to  $w_\omega \alpha$  for some non-negative weightings  $w_{c, \omega}$  and  $w_\omega$  satisfying  $\sum_\omega (w_\omega + \sum_c w_{c, \omega}) = 1$ . The weightings can be optimized for different usages. A 1-parameter subclass of weightings that contains reasonable weighting choices for many circumstances is given by  $w_{c, \omega} = (1 - w)/(C(N - 1))$  and  $w_\omega = w/(N - 1)$  for some weighting factor  $w$ . This choice of weightings results in a single  $\omega$ -independent significance threshold for the power in the individual power spectra for the  $C$  circuits of

$$T_{\text{individual}} = \text{CDF}_1^{-1} \left[ 1 - \frac{(1 - w)\alpha}{(N - 1)C} \right], \quad (8)$$

and an  $\omega$ -independent significance threshold for the power in the averaged spectrum of

$$T_{\text{average}} = \frac{1}{C} \text{CDF}_C^{-1} \left[ 1 - \frac{w\alpha}{N - 1} \right]. \quad (9)$$

All our data analysis uses these thresholds, with  $\alpha = 5\%$  and  $w = 1/2$  (with the exception of time-resolved RB, wherein  $w = 1$ , as discussed later).

**Estimating probability trajectories.** Here we explain our methods for estimating the circuit outcome probability trajectories (step 3, Fig. 1A). The methods are based on model selection, to avoid overfitting. The general form of the model that we use for a probability trajectory is:

$$p(\vec{\alpha}, t) = \alpha_0 + \sum_{\omega \in \mathbb{W}} \alpha_\omega f_\omega(t), \quad (10)$$



where  $f_\omega(t)$  is the  $\omega^{\text{th}}$  basis function of the chosen Fourier transform expressed, the summation is over some set of frequencies  $\mathbb{W}$  that are to be chosen using model selection, and the  $\alpha_\omega$  are parameters constrained only so that  $p(\vec{\alpha}, t)$  is a valid probability at all times  $t$ . In the case of the Type-II DCT the basis functions are

$$f_\omega(t) = \cos\left(\frac{\omega\pi}{N} \left[\frac{t-t_0}{t_{\text{step}}} + \frac{1}{2}\right]\right), \quad (11)$$

where, as throughout,  $t_i$  is the  $i^{\text{th}}$  data collection time for the circuit in question, and  $t_{\text{step}} = (t_{N-1} - t_0)/(N - 1)$  is the size of the time-step. The  $\alpha_i$  are constrained so that  $p(\vec{\alpha}, t)$  is within  $[0, 1]$ .

The first step is model selection to identify a set of frequencies ( $\mathbb{W}$ ). These frequencies can be chosen using the results of the hypothesis testing on the data spectra. It is useful to allow flexibility in exactly how they are chosen from the hypothesis testing results, because this allows the techniques to be adapted to different applications. A good general-purpose option, which results in estimates with a simple statistical meaning, is to set  $\mathbb{W}$  to contain those and only those frequencies that are found to be statistically significant in the power spectrum for the circuit in question. With this method we are only including frequencies that contribute a nonzero component to the true  $p(t)$  with confidence  $(1 - \alpha)$ , where  $\alpha$  is the chosen global significance level. All of the data analysis in this article uses this method, with the exception of the model selection in time-resolved RB (see later).

It remains to estimate the model parameters, *i.e.*, the amplitudes  $\vec{\alpha}$ . Maximum likelihood estimation (MLE) is a statistically sound methodology. But MLE requires a numerical optimization, which can sometimes be slow, so we also provide an optimization-free method. The data amplitude  $\hat{x}_\omega$  is a well-motivated estimate of the probability trajectory amplitude at  $\omega$ , since  $\mathbb{E}(\hat{X}_\omega) = \tilde{p}_\omega$ . In terms of the rescaled amplitudes  $\tilde{z}$ , this suggests setting  $\alpha_\omega = S(\tilde{x})\tilde{z}_\omega$  where  $S(\tilde{x})$  is a rescaling factor that inverts the normalization of the  $\tilde{z}$  amplitudes by the data standard deviation (and also rescales for the chosen normalization of the basis functions). This is intuitive but flawed: the resulting probability trajectory is not necessarily a valid probability at all times. To address this, we add an  $L_1$  regularization to this estimator. We map each amplitude via  $\alpha_\omega \rightarrow \alpha_\omega - \delta \text{sign}(\alpha_\omega)$  with  $\delta$  the smallest constant such that the new amplitudes satisfy  $\alpha_0 - \sum_{\omega \in \mathbb{W}} |\alpha_\omega| \geq \epsilon$  and  $\alpha_0 + \sum_{\omega \in \mathbb{W}} |\alpha_\omega| \leq 1 - \epsilon$  for some chosen  $\epsilon \geq 0$  (*e.g.*,  $\epsilon = 0$  if estimates on the parameter space boundary are considered acceptable). We refer to this estimation method as the *Fourier filter*, because it is a form of signal filtering. The Fourier filter returns very similar estimates to MLE under most conditions, although note that if  $\epsilon = 0$  it is possible for the Fourier filter to return estimates that have a likelihood of zero.

All data analysis in this paper uses MLE, except the time-resolved RB analysis. The motivation for using the Fourier filter in time-resolved RB is that then the speed of the analysis is limited only by the fast Fourier transform and curve fitting at the times of interest. This is particularly relevant to RB, as one motivation for using RB is its speed and simplicity.

**Model selection in time-resolved tomography.** Here we detail the model selection step in our “intrusive” approach to time-resolved tomography and benchmarking (step 5a, Fig. 1). Our methods start from a time-independent  $\{\alpha_j\}$ -parameterized model  $\mathcal{M}$  that predicts circuit outcomes. In the intrusive approach we expand each parameter  $\alpha_j$  into the

time-dependent form  $\alpha_j(t) = \alpha_{j,0} + \sum_{\omega \in \mathbb{S}_j} \alpha_{j,\omega} f_\omega(t)$ , where the  $\alpha_{j,\omega}$  are restricted only so that they satisfy any constraints on  $\alpha_j$ , the summation is over some set of non-zero frequencies  $\mathbb{S}_j$ , and  $j$  indexes all the parameters in the time-independent model. So, we obtain a new model containing  $\sum_j (|\mathbb{S}_j| + 1)$  parameters, where  $|\mathbb{S}|$  denotes the size of the set  $\mathbb{S}$ . The parameterized model is entirely defined by the set  $\mathbb{M} = \{\mathbb{S}_j\}$ , and the model selection consists of choosing this set.

For the related problem of choosing the frequencies in the model for a probability trajectory (see above) there is a clear solution: the instability detection methods are directly testing hypotheses about the frequencies in  $p(t)$ , and so there is a clear statistical justification for choosing the frequencies in our model for  $p(t)$  using the results of these tests. In contrast, the parameters in the model  $\mathcal{M}$  do not necessarily have a simple relationship to the circuit probabilities – for an arbitrary model the relationship is entirely arbitrary, and so the relationship between the frequencies detected in the probability trajectories and the frequencies in each  $\alpha_j$  is also arbitrary. However, for typical models associated with tomographic methods and circuits, *under some approximation* there is a simple relationship between the model parameters and the predicted probabilities. For the Ramsey model of Eq. (1),  $p_l(t) = A + 2\pi B \exp(-l/l_0)lt_w\Omega(t) + O((lt_w\Omega(t))^2)$ . So, if  $lt_w\Omega(t)$  is small then the dominant frequencies in  $p_l(t)$  are also necessarily frequencies in  $\Omega(t)$ . Equivalent expansions around the zero-error parameter values hold for the general process matrix model of GST (and most other tomographic techniques can be seen as a special case of GST). Therefore, we can use the results of the hypothesis tests on the data from sufficiently short circuits to select the frequencies for the model parameters. But longer circuits are more sensitive to small variations in the model parameters, so we do not want to entirely discount that data in the model selection.

To address this problem we can pick a small set of candidate models and then choose between them using the *Akaike information criterion* (AIC) [51]. For a parameterized model  $\mathcal{M}$  with  $k$  free parameters, the AIC score for that model is  $\text{AIC}(\mathcal{M}) = 2k - 2\log(\mathcal{L}_{\text{max}})$  where  $\mathcal{L}_{\text{max}}$  is the maximum of the likelihood function for that model. For a set of candidate parameterized models, the preferred model is the one with the minimum AIC score. Moreover,  $\text{AIC}(\mathcal{M}_a) - \text{AIC}(\mathcal{M}_b)$  is twice the log relative likelihood of model  $\mathcal{M}_b$  with respect to model  $\mathcal{M}_a$ , so this difference quantifies how much one model is preferred over another. This allows us to decide between multiple time-resolved models.

For the Ramsey experiment presented in the Results we select the expansion  $\Omega(t) = \alpha_0 + \sum_{\omega \in \mathbb{W}} \alpha_\omega f_\omega(t)$  where  $\mathbb{W} = \{1, 2, 3, 4, 5, 6, 7, 9, 11, 12, 13, 14, 15\}$  is the set of all the frequency indices found to be significant in any of the power spectra. We then check that the data justifies including the higher frequencies in the model (the lowest frequencies appear for  $l$  small enough so that  $lt_w\Omega(t) \approx 0$ , and so they are almost certainly components in the true  $\Omega(t)$ ). In particular, we select the 10 candidate parameterized models defined by the frequency sets  $\mathbb{W}_0 = \{1, 2, 3, 4\}$ ,  $\mathbb{W}_1 = \mathbb{W}_0 \cup \{5\}$ ,  $\mathbb{W}_2 = \mathbb{W}_1 \cup \{6\}$  through to  $\mathbb{W}_9 = \mathbb{W}$ , and compare their AIC scores,  $\text{AIC}_k$  for  $k = 1, 2, \dots, 9$ . The values of  $\text{AIC}_k - \text{AIC}_9$  are approximately 969, 421, 283, 277, 109, 97, 74, 23, 15 for  $k = 0, 1, \dots, 8$ . So the model containing all the frequencies is clearly favored according to the AIC. The detuning estimate reported in the Results is the MLE over this parameterized model.

There is no guarantee that  $\mathbb{W}$  contains all of the frequen-



cies that are components in the true  $\Omega(t)$ . We could also select some larger models to consider, but we do not do this because it would be *ad hoc*: there are  $N - 14 = 5986$  remaining frequencies that we could also include, and there is no clear method for choosing the next frequency to add. We could calculate the AIC for every possible model, but this is clearly impractical. In general, within this framework of time-resolved models based on Fourier decompositions there are  $2^{N-k}$  possible time-resolved models, where  $k$  is the number of parameters in the time-independent model. Moreover, this would not be a reasonable use of the AIC. When adding an erroneous parameter to a model sometimes the AIC score will decrease slightly due to random fluctuations in the data slightly favoring this model, and if we consider adding many different parameters this will almost certainly occur in at least one case.

**Time-resolved RB.** RB is a set of protocols for benchmarking a set of gates on  $n$  qubits [12–14]. The core protocols all follow the same general procedure:

- (i) For a range of lengths  $m$ , run  $K$  circuits sampled from some  $\Phi_m$  distribution whereby (a) the average length of a sampled circuit scales linearly with  $m$ , and (b) each circuit will deterministically output some  $n$ -bit string if implemented perfectly.
- (ii) Process the data to obtain the average success probability ( $P_m$ ) at each length  $m$ , meaning the probability that the expected bit-string was successfully output.
- (iii) Fit  $P_m$  to  $P_m = A + B\lambda^m$ , and convert  $\lambda$  to an error rate via  $r = \mathcal{N}(1 - \lambda)$  where  $\mathcal{N}$  is a constant that we set to  $\mathcal{N} = (4^n - 1)/4^n$  where  $n$  is the number of qubits.

Within this framework there are a range of different RB protocols, *e.g.*, those of Refs. [12–14], that vary in how the random circuits are chosen. Our methods can be used to upgrade any of these RB protocols to time-resolved techniques.

We focus on the non-intrusive approach to time-resolved RB, which is the following method: obtain data by rastering through the sampled circuits; use the general stability analysis to estimate the time-resolved success probability  $p(t)$  for each circuit; average the time-resolved success probabilities for all circuits of the same RB length  $m$  to obtain time-resolved average success probabilities  $P_m(t)$ ; apply the standard RB curve fitting analysis [part (iii) above] to  $P_m(t_i)$  at every time of interest  $t_i$ . The general instability analysis step in this process has some useful flexibility. It has two aspects that can be optimized to a particular task: the exact statistical hypothesis testing on the power spectra, and the selection of the frequencies to include in the time-resolved  $p(t)$  models.

Because the RB circuits are random, they are broadly all sensitive to the same physical parameters, with the exact sensitivities depending on the precise details of the random circuit. So the frequencies in  $p(t)$  will typically be the same in all the sampled circuits, even if the power in each frequency will generally vary between circuits. In this circumstance the averaged power spectrum is more powerful for detecting these frequencies, because the averaging suppresses measurement shot noise and amplifies signal *if* the same frequencies appear in most of the spectra. Moreover, here there is little penalty for erroneously including a frequency in the success probability trajectory in a few circuits – we are implementing a global analysis of the data, rather than trying to extract detailed diagnostic information. So we *only* perform hypothesis testing on the average power spectrum (*i.e.*, we set  $w = 1$  in

Eqs. (8–9)), and then we include every statistically significant frequency in the model for each success probability.

**Time-resolved RB simulation details.** In the Results we demonstrate time-resolved RB on simulated data. This demonstration is of time-resolved *direct randomized benchmarking* (DRB) [14] on two qubits, with a gate set consisting of a CPHASE gate between the qubits (*i.e.*, a controlled  $\sigma_z$ ), rotations around the  $\hat{x}$  and  $\hat{y}$  axes by  $\pm \frac{\pi}{2}$  and  $\pi$  on each qubit, and the Hadamard and idle gates on each qubit. The details of how DRB circuits are sampled (*i.e.*, the  $\Phi_m$  of DRB) can be found in Ref. [14]; they are omitted as they are not relevant to assessing the performance of time-resolved RB. We simulated gates with time-dependent coherent phase errors and time-independent depolarizing errors. Each gate is modeled as the perfect gate followed by the error map  $\mathcal{E}(t) = \mathcal{D}_\gamma \circ \mathcal{R}_z(\theta(t))$  on each qubit, where  $\mathcal{D}_\gamma[\rho] = \gamma\rho + (1 - \gamma)\mathbb{1}/2$  is a 1-qubit depolarizing map with  $\gamma = 1 - 0.04/3$  (making the probability of error 1%) and

$$\mathcal{R}_z(\phi)[\rho] = \exp\left(-i\frac{\phi}{2}\sigma_z\right)\rho\exp\left(+i\frac{\phi}{2}\sigma_z\right). \quad (12)$$

The rotation angle is set to  $\theta(t) = at + b\sin(\phi t) + c_t$  where  $a = 2\pi \times 10^{-5}$ ,  $b = 1.5 \times 10^{-2}$ ,  $\phi = 2\pi \times 10^{-2}$ , and  $c_t$  is a Brownian stochastic process given by  $c_0 = 0$  and  $c_{t+1} = c_t + \mathcal{N}(0, \nu)$  where  $\nu = 3/200$ . The parameters in this error model have been chosen to give physically plausible phase trajectories, and have no further significance. The time  $t$  starts at 0 and increases by 1 after a single run of any circuit.

In Fig. 2A the estimated time-resolved error rate is compared to the true time-dependent  $r(t)$ . The value of  $r(t)$  is obtained by fitting the *exact* instantaneous average success probabilities for the set of 100 sampled circuits. This  $r(t)$  is the target that time-resolved DRB with this particular set of random circuits is aiming for – it does *not* correspond to the  $K \rightarrow \infty$  large-sample-limit error rate that finite-sampling DRB is estimating. We choose this comparison because analysis of time-series data from one particular set of  $K$  randomly sampled circuits cannot correct for any finite sampling error introduced when sampling this set of circuits. By defining  $r(t)$  in this way, we avoid conflating this finite-circuit-sampling error with any inaccuracies that are intrinsic to time-resolved benchmarking.

**Gate set tomography.** GST is a method for jointly reconstructing a set of gates, a state preparation and a measurement [7–10]. GST is predicated on the standard *Markovian* model for errors in QIPs, whereby the prepared state is a fixed density operator, the gates are fixed *completely positive and trace preserving* (CPTP) maps – which are the linear transformations that map density operators to density operators – and the measurement is a fixed positive-operator valued measure. For our implementation of GST, we parameterize a CPTP gate by  $G = \Lambda \circ G_{\text{target}}$  where  $G_{\text{target}}$  is the fixed target map and  $\Lambda$  is a CPTP map encompassing the errors in the gate. This error map is then parameterized as  $\Lambda = \exp(G)$  with  $G$  defined by

$$G[\rho] = \sum_k \theta_k H_k[\rho] + \sum_{j,k} s_{jk} S_{jk}[\rho], \quad (13)$$

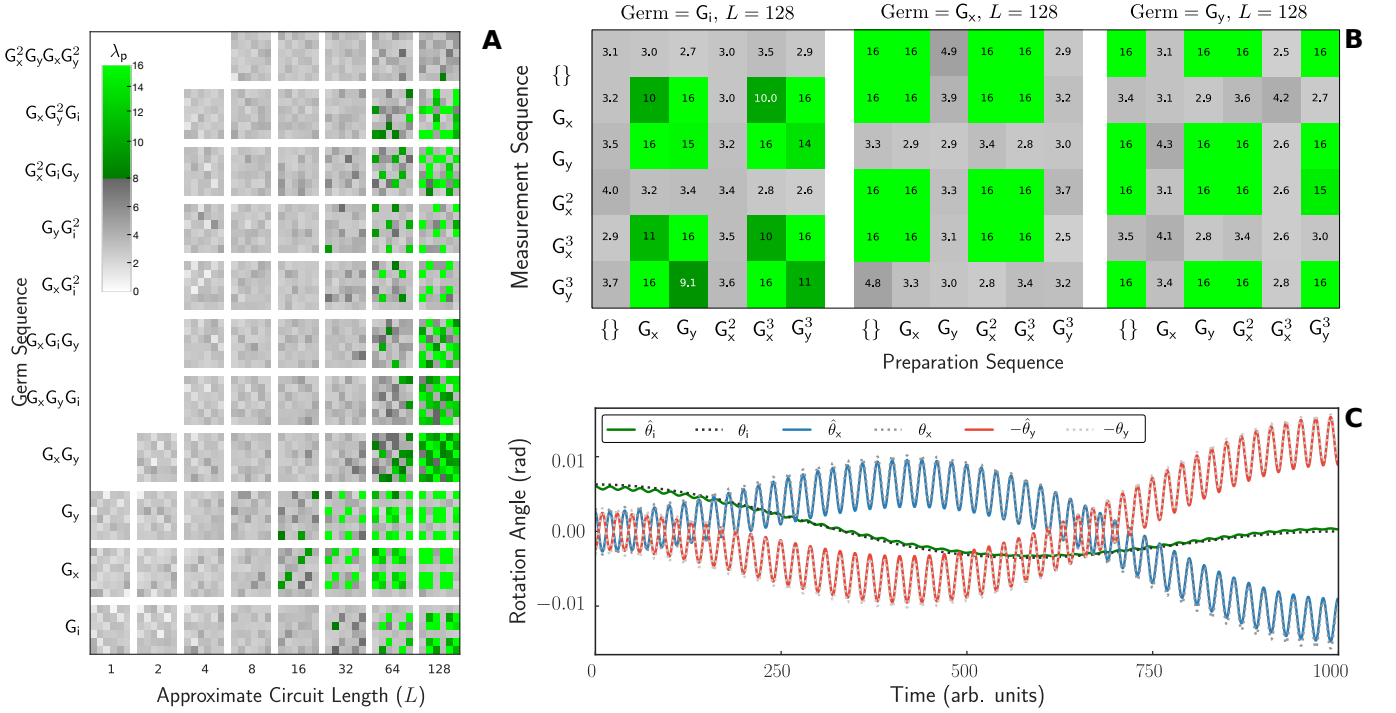


FIG. 5. **Model selection in time-resolved GST on simulated data.** **A-B.** The evidence for instability in the outcomes of each circuit in *simulated* GST data, as quantified by the test statistic  $\lambda_p$ . A pixel is colored when  $\lambda_p$  is large enough to be statistically significant, otherwise it is greyscale. The arrangement of the data is as in Fig. 3. The pattern of significant  $\lambda_p$  is used to decide which model parameters to expand into a sum of Fourier coefficients. **C.** The results of time-resolved GST when we select a time-resolved parameterized model using a simple frequency selection technique that erroneously includes high-frequency components in the  $\hat{z}$ -axis rotation angle of  $G_i$ . The parameter estimates still closely track the true values, demonstrating that time-resolved GST can be successful even with simple model selection methods.

where the summations are over  $x$ ,  $y$  and  $z$ , and

$$H_k[\rho] = \frac{i}{2}(\rho\sigma_k - \sigma_k\rho), \quad (14)$$

$$S_{jk}[\rho] = \sigma_j\rho\sigma_k - \frac{1}{2}(\rho\sigma_k\sigma_j + \sigma_k\sigma_j\rho). \quad (15)$$

Here,  $\sigma_x$ ,  $\sigma_y$  and  $\sigma_z$  are the Pauli operators. The  $\{H_k\}$  maps generate all unitary errors. If  $(\theta_x, \theta_y, \theta_z) = \phi\hat{v}$  where  $\hat{v}$  is a unit vector then the generated unitary is a rotation around the  $\hat{v}$  axis of the Bloch sphere by an angle  $\phi$ . So  $\theta_x$ ,  $\theta_y$  and  $\theta_z$  are the components of the unitary error along the  $\hat{x}$ ,  $\hat{y}$  and  $\hat{z}$  axes in the standard sense. The  $\{S_{ij}\}$  maps generate all non-unitary Markovian errors, so the matrix  $s$  dictates the stochastic error rates and the size of any amplitude damping errors. In this parameterization, the CPTP constraint is that  $s$  is positive semi-definite. Finally, note that this parameterization of  $\Lambda$  includes only infinitesimally-generated CPTP maps; it does not strictly permit every possible CPTP map.

**Time-resolved GST simulation details.** In the Results, time-resolved GST is demonstrated on simulated data. This simulated data is from GST circuits containing the gates  $G_i$ ,  $G_x$  and  $G_y$  with an error model that, when expressed in the parameterization above, consists of:

- (i) Setting the  $s$  matrix for all three gates so that if there are no coherent errors  $\Lambda$  is a uniform depolarizing channel with a 1% error rate (this is  $s \propto \mathbb{1}$ ).

- (ii) Setting all the coherent error parameters to zero, except

$$\theta_z(G_i) = \frac{2\pi}{10^3} [f_1(t) + f_2(t)],$$

$$\theta_x(G_x) = \theta_y(G_y) = \frac{4\pi}{10^3} [f_1(t) - f_2(t) + 0.5f_{100}(t)],$$

where  $\theta_k(G)$  is the  $H_k$  error rate for gate  $G$ .

Time starts at 0 and increments by 1 after each raster. The trajectories of the time-dependent parameters over the 1000 simulated rasters are shown in Fig. 2D.

To implement time-resolved GST on this simulated data we first apply the general stability analysis. The resulting  $\lambda_p = -\log_{10}(\mathbf{p})$  statistic for every circuit is shown in Fig. 6A, where  $\mathbf{p}$  is the p-value of the largest peak in the power spectrum for that circuit. (Due to numerical accuracy limitations, the minimal p-value is  $\mathbf{p} = 10^{-16}$ ). The value of  $\lambda_p$  varies strongly between circuits of the same approximate length  $L$ . The strong variations in  $\lambda_p$  imply that the time-varying errors are coherent, as stochastic errors have a fairly uniform impact across the GST circuits. Moreover, by inspecting the values of  $\lambda_p$  for the simple germs  $G_i$ ,  $G_x$  and  $G_y$  it becomes clear that  $\theta_z(G_i)$ ,  $\theta_x(G_x)$  and  $\theta_y(G_y)$  are varying. For example, with the  $G_i$  germ it is the generalized Ramsey circuits for which  $\lambda_p$  is statistically significant, as highlighted in Fig. 6B. These circuits amplify  $\theta_z(G_i)$ , so this parameter must be varying over time. Similarly, it is generalized Rabi sequences that exhibit statistically significant  $\lambda_p$  for the  $G_x$  and  $G_y$  germs, and these circuits amplify over/under-rotation errors in these gates, *i.e.*,

the parameters  $\theta_x(G_x)$  and  $\theta_y(G_y)$ . So we conclude that  $\theta_z(G_i)$ ,  $\theta_x(G_x)$  and  $\theta_y(G_y)$  should be expanded into a summation of Fourier coefficients. We now use the short-hand  $\theta_i \equiv \theta_z(G_i)$ ,  $\theta_x \equiv \theta_x(G_x)$  and  $\theta_y \equiv \theta_y(G_y)$ .

Deciding on the frequencies to include in the expansion of each of these parameters is more involved. One simple option is to use the frequencies that are statistically significant in the global power spectrum – the set  $\mathbb{W} = \{1, 2, 3, 4, 97, 98, 99, 100, 101, 102\}$  – as the frequency set for all three parameters. This parameterized model ( $\mathcal{M}_1$ ) includes all of the frequencies in the true model, but also sums and differences of these frequencies, as well as high-frequencies in the expansion of  $G_i$  that are not present in the true model. Yet, implementing MLE over this parameterized model still provides an accurate time-resolved estimate of  $\theta_i$ ,  $\theta_x$  and  $\theta_y$ , as shown in Fig. 6C.

A more sophisticated model selection strategy is to select the frequencies to include in the expansion for  $\theta_i$  (the set  $\mathbb{W}_i$ ) to be those frequencies that are statistically significant in the circuits in which  $G_i$  is a germ, and similarly for  $\theta_x$  and  $\theta_y$ . This results in the sets  $\mathbb{W}_i = \{1, 2, 3\}$ ,  $\mathbb{W}_x = \{1, 2, 3, 100, 103\}$  and  $\mathbb{W}_y = \{1, 2, 3, 5, 97, 100, 101, 103\}$ . This parameterized model ( $\mathcal{M}_2$ ) still does not contain only those frequencies that are in the true model, but each set now only contains sums and differences of the frequencies that appear in the corresponding parameter. The MLE over this parameterized model is what is reported in the Results. The difference in the AIC scores of these two candidate parameterized models is  $\text{AIC}(\mathcal{M}_1) - \text{AIC}(\mathcal{M}_2) \approx 26$ . So the AIC clearly favors discarding the erroneous frequencies in  $\mathcal{M}_1$ .

**Time-resolved GST on experimental data details.** Here we explain the exact approach used to implement time-resolved GST on the data from the first GST experiment (we implemented standard time-independent GST on the data from the second experiment). As discussed in the Results, we use the  $\lambda_p$  statistics to motivate only expanding the  $\hat{z}$ -axis rotation angle of the  $G_i$  gate – *i.e.*, using the same notation as above, the parameter  $\theta_z \equiv \theta_z(G_i)$  – into a sum of Fourier components. Specifically, we expand  $\theta_z$  into  $\theta_z = \alpha_0 + \sum_{\omega \in \mathbb{W}} \alpha_{\omega} f_{\omega}(t)$  where  $\mathbb{W} = \{1, 2, 5, 7, 15\}$  is the set of significant frequencies in the average power spectrum (shown in Fig. 3D). This method for the frequency selection is motivated by noting that, as we have decided that only  $\theta_z$  exhibits time-dependence, all the frequencies in the averaged power spectrum must be attributable to variations in  $\theta_z$ . So far this is exactly the same type of analysis as with the time-resolved GST on simulated data. However, fitting the model requires more care with experimental data.

First we implemented standard time-independent GST on all the data. The predictions of this GST estimate are compared to the aggregated counts data in Fig. 6. This summarizes the discrepancy between the data and the predictions of the model estimated by standard GST using the log-likelihood ratio (LLR) and the total variational distance (TVD). The LLR test statistic for a circuit is  $\text{LLR} = -2(\log(\mathcal{L}_{\text{gst}}/\mathcal{L}_{\text{freq}}))$ , where  $\mathcal{L}_{\text{gst}}$  is the likelihood of the outcome probabilities for that circuit predicted by the GST estimate and  $\mathcal{L}_{\text{freq}}$  is the likelihood of the outcome probabilities equal to the observed frequencies (*i.e.*, for each outcome, set the corresponding probability equal to the number of times that particular outcome was observed divided by the total number of outcome counts for the circuit). Under the null hypothesis that the model of standard GST is true, Wilks' theorem tells us that

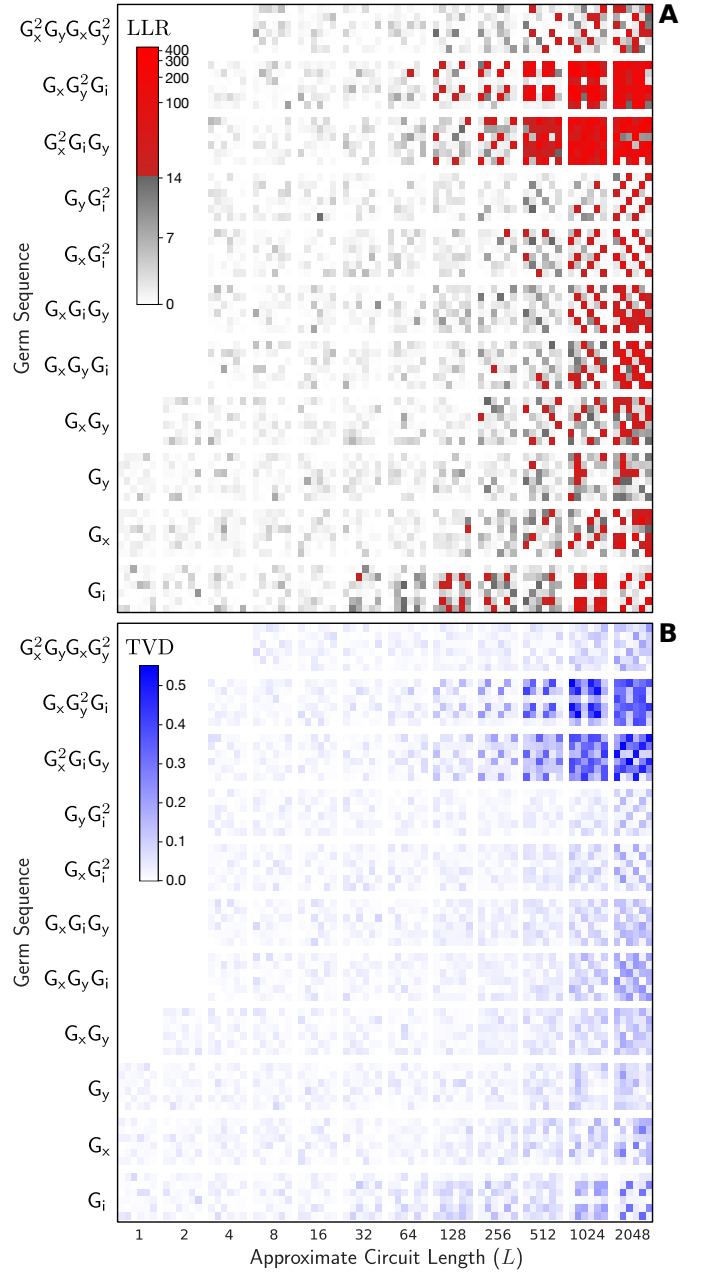


**FIG. 6. Model violation in standard GST on experimental data.** The discrepancy between the predictions of the time-independent GST estimate and the data, for the first GST experiment. **A.** The log-likelihood ratio (LLR) statistics of the GST estimate. A pixel is colored if and only if the LLR for that circuit is so large that it is inconsistent with the model of standard GST, at a global significance of 5%. **B.** The total variational distance (TVD) between the probabilities predicted by the GST estimate and the observed frequencies. The TVD is not being used as a statistic in a hypothesis test and so there is no differentiation between significant and insignificant TVDs.

the LLR is asymptotically  $\chi^2_1$  distributed. This is because, since we have many circuits, the degrees of freedom per circuit is approximately zero for the GST model (used to compute

$\mathcal{L}_{\text{gst}}$ ) and one for the model maximized over to compute  $\mathcal{L}_{\text{freq}}$ . The TVD for a circuit is  $\text{TVD} = |p_{\text{model}} - \frac{1}{N} \sum_i x_i|$ , where  $p_{\text{model}}$  is the probability for the circuit to output 1 predicted by the estimated model and  $\vec{x}$  is the clickstream for the circuit. We do not use the TVD as a test static (it has less convenient properties for hypothesis testing than the LLR), but the TVD is useful as – unlike the LLR – it quantifies the distance between the observed frequencies and the predicted probabilities. There are statistically significant LLRs in Fig. 6A, so the data are inconsistent with the model of standard GST.

From the general instability analysis, we know that there is some instability in the qubit (see Fig. 3A), so we did not expect the time-independent model of standard GST to be consistent with the data. But, if drift was the only effect outside of GST’s model that is needed to explain the data, we would expect the predictions of the estimated GST model to be inconsistent with the data only for those circuits that exhibit drift. This is not the case; comparing Fig. 6 to Fig. 3A shows that the inconsistency between the estimate of standard GST and the data *cannot* all be attributed to detectable drift. In particular, the data from many of the long circuits containing germs other than  $G_i$  are irreconcilable with the model of GST, but there is no evidence for drift in these circuits. So there is some other non-Markovian effect that our time-resolved parameterized model does not take into account.

This sort of “model violation” interferes with the model selection and data fitting techniques that we rely on. If we fit our time-resolved parameterized model to all the data, the data that are inconsistent with *any* set of parameter values can pollute the estimates and render them meaningless. So we first estimate most of the time-independent parameters in the model – specifically, the state preparation, measurement,  $G_x$ ,  $G_y$  and the non-unitary errors matrix  $s$  for the  $G_i$  – by implementing ordinary GST on the data from circuits with  $L \leq 64$  (these circuits are short enough for the model of GST to be reasonably consistent with the data). Only the two time-independent coherent error parameters in  $G_i$  and  $\theta_z$  – which is a summation of 6 Fourier coefficients – are not fixed by this initial fit. Using MLE, we then fit this 8-parameter time-resolved model to the time-series data for all circuits with  $L \leq 64$  and all the circuits where  $G_i$  is a germ with  $L \leq 1024$ . This allows us to extract information about the time-dependent parameter without polluting the results with data that does not fit this model.

In the Results, we report the diamond distance error rate ( $\epsilon_\diamond$ ) of the estimated (time-resolved) gate process matrices. Table I includes additional information on the gate error rates. In addition to  $\epsilon_\diamond$ , this table reports the entanglement infidelity ( $\epsilon_f$ ) and spectral entanglement infidelity ( $\epsilon_{\text{spec},f}$ ) for each gate. The diamond distance error rate for process matrix  $G$  is  $\epsilon_\diamond = \frac{1}{2} \|G - G_{\text{target}}\|_\diamond$  where  $\|\cdot\|_\diamond$  is the diamond norm [66]. The entanglement infidelity is  $\epsilon_f = 1 - \langle \varphi | (\mathbb{1} \otimes G G_{\text{target}}^\dagger)(\varphi) | \varphi \rangle$  where  $\varphi$  is any maximally entangled state [67]. The spectral entanglement infidelity is the entanglement infidelity between  $\text{Spec}(G)$  and  $\text{Spec}(G_{\text{target}})$  where  $\text{Spec}(A)$  is the diagonal matrix that has the eigenvalues of the matrix  $A$  on the diagonal (and the relative ordering of the eigenvalues in the two matrices is chosen to minimize  $\epsilon_{\text{spec},f}$ ). The spectral entanglement infidelity is a alternative to the standard entanglement infidelity that is invariant under transformation of the “GST gauge” (see Ref. [7] for discussions of this gauge).

Error rate	$\epsilon_\diamond \times 10^3$		$\epsilon_f \times 10^3$		$\epsilon_{\text{spec},f} \times 10^3$	
Exp. #	1	2	1	2	1	2
$G_i$	3.5	0.40	0.02	0.07	0.02	0.07
$G_x$	4.7	0.38	0.03	0.06	0.03	0.06
$G_y$	4.0	0.53	0.15	0.04	0.15	0.04

TABLE I. **Estimated gate error rates.** Error rates for the three gates in the two GST experiments, obtained using time-resolved GST. In the first experiment the error rates of the  $G_i$  gate vary over time (see Fig. 3C). The values reported here are the average over the experiment duration. All other error rates are static over the course of each experiment.

**Analyzing data from circuits with more than 2 outcomes.** Throughout this article we have only considered analysis of circuits with 0/1 outcomes, which is sufficient for all the experiments and simulations herein. However, the techniques we present can be easily generalized to  $M$ -outcome circuits, as we now briefly outline. In this more general setting, the aim is still to detect and quantify time variation in the probability distribution over outcomes for each circuit. However  $M$  can be very large in commonly encountered circumstances, as  $M = 2^n$  for an  $n$ -qubit circuit terminated with the standard measurement. Even accurate estimation of a time-independent distribution over a very large number of outcomes is infeasible with reasonable quantities of data, so it will not be possible to accurately estimate a time-dependent distribution with many outcomes. For this reasons, it is useful to allow for a coarse-graining of the outcomes into  $\tilde{M} \leq M$  bins (*e.g.*, we can marginalize over some subset of the qubits in an  $n$ -qubit circuit or bin the outcomes into two sets). The analysis will then interrogate time-dependence in the coarse-grained probability distribution. So coarse-graining can make the analysis feasible with a reasonable amount of data, but the analysis will be insensitive to any time dependence that disappears under the chosen coarse-graining.

Each coarse-grained outcome has a bit-string time-series associated with it, corresponding to whether or not that measurement outcome was observed at each time. A power spectrum can be calculated for each such bit-string, and exactly the same hypothesis testing performed on each such power spectrum as in the 0/1 outcomes cases (with an appropriate correction for the increased number of hypothesis tests). Moreover, the spectrum obtained by averaging the spectra for a circuit over coarse-grained measurement outcomes can also be tested (which will be approximately  $\chi^2_{\tilde{M}-1}$  distributed under the null hypothesis), or tested instead of the per-outcome spectra to avoid significance dilution by implementing too many hypothesis tests. The probability trajectory estimation (step 3, Fig. 1A) then proceeds exactly as in the 0/1 outcome case, except that now the estimation is of  $\tilde{M}$  trajectories that must sum to 1 at all times. Any time-resolved parameter estimation proceeds exactly as in the 0/1 outcome case.

**Data availability.** The data is available upon request. The data analysis was performed using the **drift** module of the open-source Python package **pyGSTi** [56], which was developed for this work. The tutorial Jupyter notebooks included with **pyGSTi** detail how to use the code to implement the same or similar data analysis routines to those presented herein.



## ACKNOWLEDGMENTS

This work was supported by the U.S. Department of Energy, Office of Science, Office of Advanced Scientific Computing Research Quantum Testbed Program; the Office of the Director of National Intelligence (ODNI), Intelligence Advanced Research Projects Activity (IARPA); and the Laboratory Directed Research and Development program at Sandia National Laboratories. Sandia National Laboratories is a multi-program laboratory managed and operated by National Technology and Engineering Solutions of Sandia, LLC., a wholly owned subsidiary of Honeywell International, Inc., for the U.S. Department of Energy's National Nuclear Security Administration under contract DE-NA-0003525. All statements of fact, opinion or conclusions contained herein are those of the authors and should not be construed as representing the official views or policies of IARPA, the ODNI, the U.S. Department of Energy, or the U.S. Government.

## AUTHOR CONTRIBUTIONS

T.P., E.N., K.R., R.B.-K. and K.Y. developed the methods. M.R., D.L., and P.M. performed the experiments.

---

\* tjproct@sandia.gov

- [1] MA Rol, CC Bultink, TE O'Brien, SR de Jong, LS Theis, X Fu, F Luthi, RFL Vermeulen, JC de Sterke, A Bruno, *et al.*, "Restless tuneup of high-fidelity qubit gates," *Phys. Rev. Appl.* **7**, 041001 (2017).
- [2] JS Otterbach, R Manenti, N Alidoust, A Bestwick, M Block, B Bloom, S Caldwell, N Didier, E Schuyler Fried, S Hong, *et al.*, "Unsupervised machine learning on a hybrid quantum computer," *arXiv preprint arXiv:1712.05771* (2017).
- [3] Nicolai Friis, Oliver Marty, Christine Maier, Cornelius Hempel, Milan Holzapfel, Petar Jurcevic, Martin B Plenio, Marcus Huber, Christian Roos, Rainer Blatt, *et al.*, "Observation of entangled states of a fully controlled 20-qubit system," *Phys. Rev. X* **8**, 021012 (2018).
- [4] Julian Kelly, "Engineering superconducting qubit arrays for quantum supremacy," *Bulletin of the American Physical Society* (2018).
- [5] Intel, "2018 CES: Intel advances quantum and neuromorphic computing research," (2018), URL: <https://newsroom.intel.com/news/intel-advances-quantum-neuromorphic-computing-research/>.
- [6] IBM, "IBM Quantum Experience," URL: <https://quantumexperience.ng.bluemix.net/qx/devices>.
- [7] Robin Blume-Kohout, John King Gamble, Erik Nielsen, Kenneth Rudinger, Jonathan Mizrahi, Kevin Fortier, and Peter Maunz, "Demonstration of qubit operations below a rigorous fault tolerance threshold with gate set tomography," *Nat. Commun.* **8**, 14485 (2017).
- [8] Seth T Merkel, Jay M Gambetta, John A Smolin, Stefano Poletto, Antonio D Córcoles, Blake R Johnson, Colm A Ryan, and Matthias Steffen, "Self-consistent quantum process tomography," *Phys. Rev. A* **87**, 062119 (2013).
- [9] Robin Blume-Kohout, John King Gamble, Erik Nielsen, Jonathan Mizrahi, Jonathan D Sterk, and Peter Maunz, "Robust, self-consistent, closed-form tomography of quantum logic gates on a trapped ion qubit," *arXiv preprint arXiv:1310.4492* (2013).
- [10] Daniel Greenbaum, "Introduction to quantum gate set tomography," *arXiv preprint arXiv:1509.02921* (2015).
- [11] Shelby Kimmel, Guang Hao Low, and Theodore J Yoder, "Robust calibration of a universal single-qubit gate set via robust phase estimation," *Phys. Rev. A* **92**, 062315 (2015).
- [12] Emanuel Knill, D Leibfried, R Reichle, J Britton, RB Blakestad, JD Jost, C Langer, R Ozeri, S Seidelin, and DJ Wineland, "Randomized benchmarking of quantum gates," *Phys. Rev. A* **77**, 012307 (2008).
- [13] Easwar Magesan, Jay M Gambetta, and Joseph Emerson, "Scalable and robust randomized benchmarking of quantum processes," *Phys. Rev. Lett.* **106**, 180504 (2011).
- [14] Timothy J Proctor, Arnaud Carignan-Dugas, Kenneth Rudinger, Erik Nielsen, Robin Blume-Kohout, and Kevin Young, "Direct randomized benchmarking for multi-qubit devices," *Phys. Rev. Lett.* **123** (2019).
- [15] Easwar Magesan, Jay M Gambetta, Blake R Johnson, Colm A Ryan, Jerry M Chow, Seth T Merkel, Marcus P da Silva, George A Keefe, Mary B Rothwell, Thomas A Ohki, *et al.*, "Efficient measurement of quantum gate error by interleaved randomized benchmarking," *Phys. Rev. Lett.* **109**, 080505 (2012).
- [16] Andrew W Cross, Easwar Magesan, Lev S Bishop, John A Smolin, and Jay M Gambetta, "Scalable randomized benchmarking of non-clifford gates," *NPJ Quantum Inf.* **2**, 16012 (2016).
- [17] R Barends, J Kelly, A Veitia, A Megrant, AG Fowler, B Campbell, Y Chen, Z Chen, B Chiaro, A Dunsworth, *et al.*, "Rolling quantum dice with a superconducting qubit," *Phys. Rev. A* **90**, 030303 (2014).
- [18] Arnaud Carignan-Dugas, Joel J Wallman, and Joseph Emerson, "Characterizing universal gate sets via dihedral benchmarking," *Phys. Rev. A* **92**, 060302 (2015).
- [19] Jay M Gambetta, AD Córcoles, Seth T Merkel, Blake R Johnson, John A Smolin, Jerry M Chow, Colm A Ryan, Chad Rigetti, S Poletto, Thomas A Ohki, *et al.*, "Characterization of addressability by simultaneous randomized benchmarking," *Phys. Rev. Lett.* **109**, 240504 (2012).
- [20] Juan P Dehollain, Juha T Muhonen, Robin Blume-Kohout, Kenneth M Rudinger, John King Gamble, Erik Nielsen, Arne Laucht, Stephanie Simmons, Rachpon Kalra, Andrew S Dzurak, *et al.*, "Optimization of a solid-state electron spin qubit using gate set tomography," *New J. Phys.* **18**, 103018 (2016).
- [21] Jeffrey M Epstein, Andrew W Cross, Easwar Magesan, and Jay M Gambetta, "Investigating the limits of randomized benchmarking protocols," *Phys. Rev. A* **89**, 062321 (2014).
- [22] Steven J van Enk and Robin Blume-Kohout, "When quantum tomography goes wrong: drift of quantum sources and other errors," *New J. Phys.* **15**, 025024 (2013).
- [23] Bryan H Fong and Seth T Merkel, "Randomized benchmarking, correlated noise, and ising models," *arXiv preprint arXiv:1703.09747* (2017).
- [24] MA Fogarty, M Veldhorst, R Harper, CH Yang, SD Bartlett, ST Flammia, and AS Dzurak, "Nonexponential fidelity decay in randomized benchmarking with

- low-frequency noise,” *Phys. Rev. A* **92**, 022326 (2015).
- [25] JM Chow, Jay M Gambetta, Lars Tornberg, Jens Koch, Lev S Bishop, Andrew A Houck, BR Johnson, L Frunzio, Steven M Girvin, and Robert J Schoelkopf, “Randomized benchmarking and process tomography for gate errors in a solid-state qubit,” *Phys. Rev. Lett.* **102**, 090502 (2009).
- [26] Yong Wan, Daniel Kienzler, Stephen D Erickson, Karl H Mayer, Ting Rei Tan, Jenny J Wu, Hilma M Vasconcelos, Scott Glancy, Emanuel Knill, David J Wineland, *et al.*, “Quantum gate teleportation between separated zones of a trapped-ion processor,” *arXiv preprint arXiv:1902.02891* (2019).
- [27] R Harris, MW Johnson, S Han, AJ Berkley, J Johansson, P Bunyk, E Ladizinsky, S Govorkov, MC Thom, S Uchaikin, *et al.*, “Probing noise in flux qubits via macroscopic resonant tunneling,” *Phys. Rev. Lett.* **101**, 117003 (2008).
- [28] Jonas Bylander, Simon Gustavsson, Fei Yan, Fumiki Yoshihara, Khalil Harrabi, George Fitch, David G Cory, Yasunobu Nakamura, Jaw-Shen Tsai, and William D Oliver, “Noise spectroscopy through dynamical decoupling with a superconducting flux qubit,” *Nature Physics* **7**, 565 (2011).
- [29] KW Chan, W Huang, CH Yang, JCC Hwang, B Hensen, T Tanttu, FE Hudson, Kohei M Itoh, A Laucht, A Morello, *et al.*, “Assessment of a silicon quantum dot spin qubit environment via noise spectroscopy,” *Phys. Rev. Appl.* **10**, 044017 (2018).
- [30] PV Klimov, Julian Kelly, Z Chen, Matthew Neeley, Anthony Megrant, Brian Burkett, Rami Barends, Kunal Arya, Ben Chiaro, Yu Chen, *et al.*, “Fluctuations of energy-relaxation times in superconducting qubits,” *Phys. Rev. Lett.* **121**, 090502 (2018).
- [31] Anthony Megrant, Charles Neill, Rami Barends, Ben Chiaro, Yu Chen, Ludwig Feigl, Julian Kelly, Erik Lucero, Matteo Mariantoni, Peter JJ O’Malley, *et al.*, “Planar superconducting resonators with internal quality factors above one million,” *Appl. Phys. Lett.* **100**, 113510 (2012).
- [32] Clemens Müller, Jürgen Lisenfeld, Alexander Shnirman, and Stefano Poletto, “Interacting two-level defects as sources of fluctuating high-frequency noise in superconducting circuits,” *Phys. Rev. B* **92**, 035442 (2015).
- [33] Saskia M Meißner, Arnold Seiler, Jürgen Lisenfeld, Alexey V Ustinov, and Georg Weiss, “Probing individual tunneling fluctuators with coherently controlled tunneling systems,” *Phys. Rev. B* **97**, 180505 (2018).
- [34] SE De Graaf, L Faoro, J Burnett, AA Adamyan, A Ya Tzalenchuk, SE Kubatkin, T Lindström, and AV Danilov, “Suppression of low-frequency charge noise in superconducting resonators by surface spin desorption,” *Nat. Commun.* **9**, 1143 (2018).
- [35] B Merkel, K Thirumalai, JE Tarlton, VM Schäfer, CJ Ballance, TP Harty, and DM Lucas, “Magnetic field stabilization system for atomic physics experiments,” *arXiv preprint arXiv:1808.03310* (2018).
- [36] Jonathan Burnett, Andreas Bengtsson, Marco Scigliuzzo, David Niepce, Marina Kudra, Per Delsing, and Jonas Bylander, “Decoherence benchmarking of superconducting qubits,” *arXiv preprint arXiv:1901.04417* (2019).
- [37] Luis Cortez, Areeya Chantasri, Luis Pedro García-Pintos, Justin Dressel, and Andrew N Jordan, “Rapid estimation of drifting parameters in continuously measured quantum systems,” *Phys. Rev. A* **95**, 012314 (2017).
- [38] Cristian Bonato and Dominic W Berry, “Adaptive tracking of a time-varying field with a quantum sensor,” *Physical Review A* **95**, 052348 (2017).
- [39] TA Wheatley, DW Berry, H Yonezawa, D Nakane, H Arao, DT Pope, TC Ralph, HM Wiseman, A Furusawa, and EH Huntington, “Adaptive optical phase estimation using time-symmetric quantum smoothing,” *Phys. Rev. Lett.* **104**, 093601 (2010).
- [40] Kevin C Young and K Birgitta Whaley, “Qubits as spectrometers of dephasing noise,” *Phys. Rev. A* **86**, 012314 (2012).
- [41] Riddhi Swaroop Gupta and Michael J Biercuk, “Machine learning for predictive estimation of qubit dynamics subject to dephasing,” *Physical Review Applied* **9**, 064042 (2018).
- [42] Christopher Granade, Joshua Combes, and DG Cory, “Practical bayesian tomography,” *New J. Phys.* **18**, 033024 (2016).
- [43] Christopher Granade, Christopher Ferrie, Ian Hincks, Steven Casagrande, Thomas Alexander, Jonathan Gross, Michal Kononenko, and Yuval Sanders, “Qinfer: Statistical inference software for quantum applications,” *Quantum* **1**, 5 (2017).
- [44] Ming-Xia Huo and Ying Li, “Learning time-dependent noise to reduce logical errors: Real time error rate estimation in quantum error correction,” *New J. Phys.* **19**, 123032 (2017).
- [45] J Kelly, R Barends, AG Fowler, A Megrant, E Jeffrey, TC White, D Sank, JY Mutus, B Campbell, Yu Chen, *et al.*, “Scalable in situ qubit calibration during repetitive error detection,” *Phys. Rev. A* **94**, 032321 (2016).
- [46] Mingxia Huo and Ying Li, “Temporally correlated error tomography and mitigation in quantum computer,” *arXiv preprint arXiv:1811.02734* (2018).
- [47] Kenneth Rudinger, Timothy Proctor, Dylan Langharst, Mohan Sarovar, Kevin Young, and Robin Blume-Kohout, “Probing context-dependent errors in quantum processors,” *Phys. Rev. X* **9**, 021045 (2019).
- [48] David L Donoho, “Compressed sensing,” *IEEE Trans. Inf. Theory* **52**, 1289–1306 (2006).
- [49] Erich L Lehmann and Joseph P Romano, *Testing statistical hypotheses* (Springer Science & Business Media, 2006).
- [50] Juliet Popper Shaffer, “Multiple hypothesis testing,” *Annual review of psychology* **46**, 561–584 (1995).
- [51] Hirotugu Akaike, “A new look at the statistical model identification,” *IEEE Trans. Autom. Control* , 716–723 (1974).
- [52] Stephen Wimperis, “Broadband, narrowband, and pass-band composite pulses for use in advanced nmr experiments,” *J. Magn. Reson. Series A* **109**, 221–231 (1994).
- [53] J Merrill and Kenneth R Brown, “Progress in compensating pulse sequences for quantum computation,” *arXiv preprint arXiv:1203.6392* (2012).
- [54] Kaveh Khodjasteh and Lorenza Viola, “Dynamical quantum error correction of unitary operations with bounded controls,” *Phys. Rev. A* **80**, 032314 (2009).
- [55] Dorit Aharonov, Alexei Kitaev, and Noam Nisan, “Quantum circuits with mixed states,” in *Proceedings of the thirtieth annual ACM symposium on Theory of computing* (ACM, 1998) pp. 20–30.
- [56] Erik Nielsen, Robin Blume-Kohout, Lucas Saldyt, Jonathan Gross, Travis Scholten, Kenneth Rudinger,

- Timothy Proctor, and John King Gamble, “PyGSTi version 0.9.8,” (2019), 10.5281/zenodo.3262737.
- [57] Peter TH Fisk, MJ Sellars, Malcolm A Lawn, and G Coles, “Accurate measurement of the 12.6 GHz “clock” transition in trapped  $^{71}\text{Yb}^+$  ions,” *IEEE Trans. Ultrasonics, Ferroelectrics, and Frequency Control* **44**, 344–354 (1997).
  - [58] Steve Olmschenk, Kelly C Younge, David L Moehring, Dzmitry N Matsukevich, Peter Maunz, and Christopher Monroe, “Manipulation and detection of a trapped  $\text{Yb}^+$  hyperfine qubit,” *Phys. Rev. A* **76**, 052314 (2007).
  - [59] K Ramamohan Rao and Ping Yip, *Discrete cosine transform: algorithms, advantages, applications* (Academic press, 2014).
  - [60] Nasir Ahmed, T. Natarajan, and Kamisetty R Rao, “Discrete cosine transform,” *IEEE Trans. Comput.* **100**, 90–93 (1974).
  - [61] Frank A Feldman, “Fast spectral tests for measuring non-randomness and the DES,” in *Conference on the Theory and Application of Cryptographic Techniques* (Springer, 1987) pp. 243–254.
  - [62] M Zechmeister and M Kürster, “The generalised Lomb-Scargle periodogram – a new formalism for the floating-mean and keplerian periodograms,” *Astron. Astrophys.* **496**, 577–584 (2009).
  - [63] Jacob T VanderPlas, “Understanding the Lomb–Scargle periodogram,” *Astro. J. Supplement Series* **236**, 16 (2018).
  - [64] Yoav Benjamini and Yosef Hochberg, “Controlling the false discovery rate: a practical and powerful approach to multiple testing,” *J. Roy. Statist. Soc. Ser. B*, 289–300 (1995).
  - [65] Patrick Billingsley, *Probability and measure*, 3rd ed. (John Wiley & Sons, 1995).
  - [66] John Watrous, “Notes on super-operator norms induced by Schatten norms,” *Quantum Information & Computation* **5**, 58–68 (2005).
  - [67] Michael A Nielsen, “A simple formula for the average gate fidelity of a quantum dynamical operation,” *Phys. Lett. A* **303**, 249–252 (2002).